Geochemistry 85 (2025) 126355

Contents lists available at ScienceDirect

Geochemistry

journal homepage: www.elsevier.com/locate/chemer

Major and trace element geochemistry and Sr–Nd isotopic constraints on mafic volcanic rocks from the Ventura-Espiritu Santo Volcanic Field, San Luis Potosi, Mexico: Petrogenesis and tectonic implications of Cenozoic volcanism in the Basin and Range Province

Karla R. Hernández Martínez [a], Sanjeet K. Verma [a,*], Darío Torres-Sánchez [b], Erik Emmanuel M. Torres [a], José R. Torres Hernández [c], Sonia A. Torres-Sánchez [d], Hector Hernández-Mendoza [e], Juan Antonio Moreno [f], José Manuel Fuenlabrada [g], Beatriz A. Rivera-Escoto [h]

[a] División de Geociencias Aplicadas, Instituto Potosino de Investigación Científica y Tecnológica (IPICYT), Camino a la Presa San José 2055, San Luis Potosí, 78216, Mexico
[b] Instituto de Geociencias, UNAM Campus Juriquilla, Blvd. Juriquilla No. 3001, Querétaro, 76230, Mexico
[c] Instituto de Geología, Universidad Autónoma de San Luis Potosí, Manuel Nava No. 5 Zona Universitaria, 78240, San Luis Potosí, Mexico
[d] Facultad de Ingeniería, Área de Geología, Universidad Autónoma de San Luis Potosí, Manuel Nava No. 5 Zona Universitaria, 78240, San Luis Potosí, Mexico
[e] Instituto de Investigación de Zonas Desérticas, Universidad Autónoma de San Luis Potosí, Altair 200, CP 78377, San Luis, S.L.P., Mexico
[f] Departamento de Ciencias de la Tierra, Universidad de Huelva, Campus de El Carmen, 21071, Huelva, Spain
[g] Unidad de Geocronología (CAI de Ciencias de la Tierra y Arqueometría), Universidad Complutense de Madrid, Avenida Séneca 2, 28040, Madrid, Spain
[h] División de Materiales Avanzados, Instituto Potosino de Investigación en Ciencia y Tecnología (IPICYT), Camino a la Presa San José # 2055, Col. Lomas 4a Sec., San Luis Potosí, SLP, 78216, Mexico

ARTICLE INFO

Handling Editor: Federico Lucci

Keywords:
Mafic rocks
Sr–Nd isotopic geochemistry
Petrogenesis
Plio-quaternary
Extensional regime

ABSTRACT

The Ventura Espiritu Santo Volcanic Field (VESVF), located in the central part of the Mesa Central (MC), Mexico, is a monogenetic volcanic field dominated by Late Pleistocene mafic volcanism. It covers an area of approximately 100 km between the localities of Cúcamo and Santa Lucia and is emplaced on a basement composed of metamorphic rocks of the Sierra de Salinas and Triassic marine sequences that are tectonically overlain by the Guerrero Terrane. This study presents new petrographic observations, whole-rock major-and trace-element geochemistry, and Sr-Nd isotopic data for mafic rocks from the Cúcamo, El Rosario, and Santa Lucía areas to constrain the magmatic processes involved in the origin and evolution. Chondrite-normalized REE patterns display moderate enrichment in Light Rare Earth Elements (LREE) accompanied by slight depletion in Heavy Rare Earth Elements (HREE) and absence of an Eu anomaly. Primitive mantle-normalized diagrams show prominent positive anomalies in K, P, and Ti, together with negative anomalies in Pb. The absence of Nb-Ta troughs, together with multidimensional discrimination diagrams, could indicate an affinity to intraplate geochemical signature. Isotopic composition ($^{87}Sr/^{86}Sr_i$ = [0.70307–0.70353, εNd = +5.8 to +6.3] suggests derivation from an enriched mantle source. The trace-element behavior, supported by geochemical modeling, further indicates that the mafic rocks were generated by low degree of partial melting of the enriched lherzolite upper lithospheric mantle source, pointing to a tectonic environment dominated by lithospheric extension and asthenospheric upwelling.

1. Introduction

The Basin and Range Province (BRP) is a physiographic region covering much of the western part of the United States and northwestern Mexico (Fig. 1a). The BRP was formed by an extensional deformation during the Cenozoic (Dickinson, 2002). In its southern sector (western

* Corresponding author.
E-mail addresses: sanjeet.verma@ipicyt.edu.mx, sanjeet_vrm@yahoo.com (S.K. Verma).

https://doi.org/10.1016/j.chemer.2025.126355
Received 30 April 2025; Received in revised form 10 November 2025; Accepted 16 November 2025
Available online 24 November 2025

United States and northwestern Mexico), this extension is linked to the displacement of the Rivera Triple Junction (RTJ) at the southern tip of the Baja California Peninsula (Dickinson, 2004). Furthermore, extensional tectonic activity across much of Mexico has been expressed through mafic intraplate magmatism from Miocene to the Plio-Quaternary. Comparable, intraplate mafic rocks are particularly abundant in the Northern Extensional Province of Mexico, showing a tectono-magmatic evolution similar to that of the Mesa Central (Luhr et al., 2006; Torres-Sánchez et al., 2020).

The Mesa Central (MC) is a major physiographic province located within the southern part of the BRP in Mexico (Fig. 1a; Nieto-Samaniego et al., 2007). The MC forms a prominent plateau that can be subdivided into two distinct domains: (1) the northern domain, which is characterized by Mesozoic marine sedimentary rocks deformed during the Mexican Laramide (Fitz-Díaz et al., 2018; Nieto-Samaniego et al., 2023); and (2) the southern domain, composed primarily of Miocene to Pleistocene volcanic rocks cross-cut by several normal faults (Fig. 1a; Nieto-Samaniego et al., 1999; Nieto-Samaniego et al., 2007). The San Luis Potosí Volcanic Complex (SLPVC) is located in the east-central portion of the MC and is composed of volcanic rocks ranging in age from the middle Eocene to the Plio-Quarter nary, including basalts, andesites, and rhyolites (Tristán–González et al., 2009; Torres-Sánchez et al., 2020). Within the SLPVC, several volcanic fields have been identified (Fig. 1b): (i) the Santo Domingo Volcanic Field (SDVF; Luhr et al., 1989; Luhr and Aranda-Gómez, 1997; Dávalos-Elizondo et al., 2016), (ii) the Ventura-Espíritu Santo Volcanic Field (VESVF; Luhr et al., 1989; Luhr and Aranda-Gómez, 1997), and (iii) the Los Encinos Volcanic Field (LEVF; Luhr et al., 1995a). These volcanic fields, particularly the SDVF, VESVF, and LEVF, have been previously studied by Luhr et al. (1989, 1995a), Luhr and Aranda-Gómez (1997), and Dávalos-Elizondo et al. (2016). These studies provided detailed mineralogical and geochemical analyses and describe the evolution and magmatic processes of maars and mafic volcanic rocks, especially within the southern sector of the VESVF (Fig. 1b). However, these studies have reported geochemical data (major and trace elements), they did not fully investigate the magmatic genesis and evolution in the conditions of volcanism in the northwestern VESVF. Therefore, the main objective of this work is to address the underexplored problem of magma genesis in the northwestern sector of the VESVF, where mafic volcanic rocks from the Cúcamo and El Zacatón areas (including El Rosario and Santa Lucía) have been documented. In this work, we present new petrographic observations, geochemistry of major and trace element geochemistry as well as isotopic data (Sr–Nd) of these mafic rocks to understand their magma generation processes and assess their geodynamic.

2. Geological setting

The VESVF is a monogenetic volcanic field, characterized by alkaline-subalkaline volcanic activity that developed during the Late Pleistocene. The basement underlying the volcanic fields in the MC consists of metamorphic rocks exposed in the Sierra de Salinas and a marine calcareous clay sequence of Triassic age known as the Zacatecas Formation. This sequence is tectonically overlain by the Guerrero Terrane, which formed during the Upper Jurassic to Lower Cretaceous age (Centeno-García et al., 2008, 2011; Centeno-García, 2017). The Guerrero terrane is a composite block composed of five distinct units (Centeno-García et al., 2008). The Teloloapan terrane consists of Lower Cretaceous island-arc andesitic to basaltic lava flows, interbedded with limestone and volcaniclastic rocks. The Guanajuato and Arcelia terranes are characterized by Lower Cretaceous supra-subduction ophiolite successions. The Tahue terrane represents a Paleozoic accreted arc and associated sedimentary sequences whereas the Zihuatanejo terrane comprises Triassic ocean-flank to ocean-floor assemblages accreted in Early Jurassic. The study area (Fig. 2) is characterized by a crustal assemblage of the Sierra Madre and Guerrero tectonostratigraphic terranes. Theses terranes correspond to a Grenvillian granulitic basement (Oaxaquia) on which an Upper Triassic siliciclastic sequence in the form of a submarine fan called "Potosí Fan" accumulated unconformably (Centeno-García, 2005, 2017). The southern part of the MC (Fig. 1b) is covered by volcanic fields from the middle and late Cenozoic (Nieto-Samaniego et al., 1999, 2007), made up mainly of felsic rocks (rhyolites and dacites) in form of lavas and ignimbrites, with minor presence of mafic rocks. Basaltic and rhyolitic lavas from the early Miocene are found scattered (Torres-Hernández et al., 2006). Furthermore, in the middle Miocene (~12 Ma), after a long hiatus (early to middle Miocene) in volcanism, the emission of intraplate type alkaline mafic rocks began in the LEVF, and later, effusive volcanism and phreatomagmatism type, have formed the VESVF and SDVF. This volcanism during the Miocene and Plio-Quaternary that built several volcanic fields (LEVF and VESVF/SDVF, respectively) have been widely studied by different authors (Luhr and Aranda-Gómez, 1997; Aranda-Gómez et al., 2005; Paz-Moreno et al., 2003; Dávalos-Elizondo et al., 2016). The VESVF spans an extensive area of approximately 100 km, extending between the localities of Cúcamo and Santa Lucía (Fig. 2) and is characterized by many isolated cinder cones and associated mafic lava flows, which align along a preferential east–west (E–W) trending system of normal faults (Luhr et al., 1989; Luhr and Aranda-Gómez, 1997). These structures are associated with an extensional tectonic regime that is likely controlled the spatial distribution of volcanism in the area (Fig. 2; e.g., Luhr et al.,

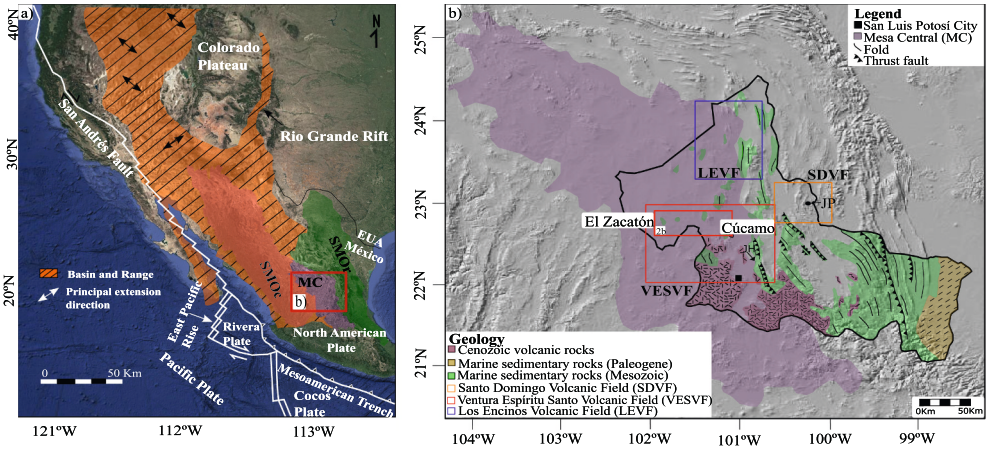

Fig. 1. (a) Regional tectonic map of western North America and the Basin and Range Province (BRP) modified after Torres-Sánchez et al. (2020), the location of geological provinces such as the), Mesa Central (MC), Sierra Madre Oriental (SMOr) and Sierra Madre Occidental (SMO) taken and modified after Torres-Sánchez et al. (2019); b) Generalized geological map of the MC province showing the location volcanic fields in the San Luis Potosi modified after Aranda-Gómez et al. (2005). Abbreviation: JP– Joya Prieta, JH–Joya Honda, and SLP–San Luis Potosi.

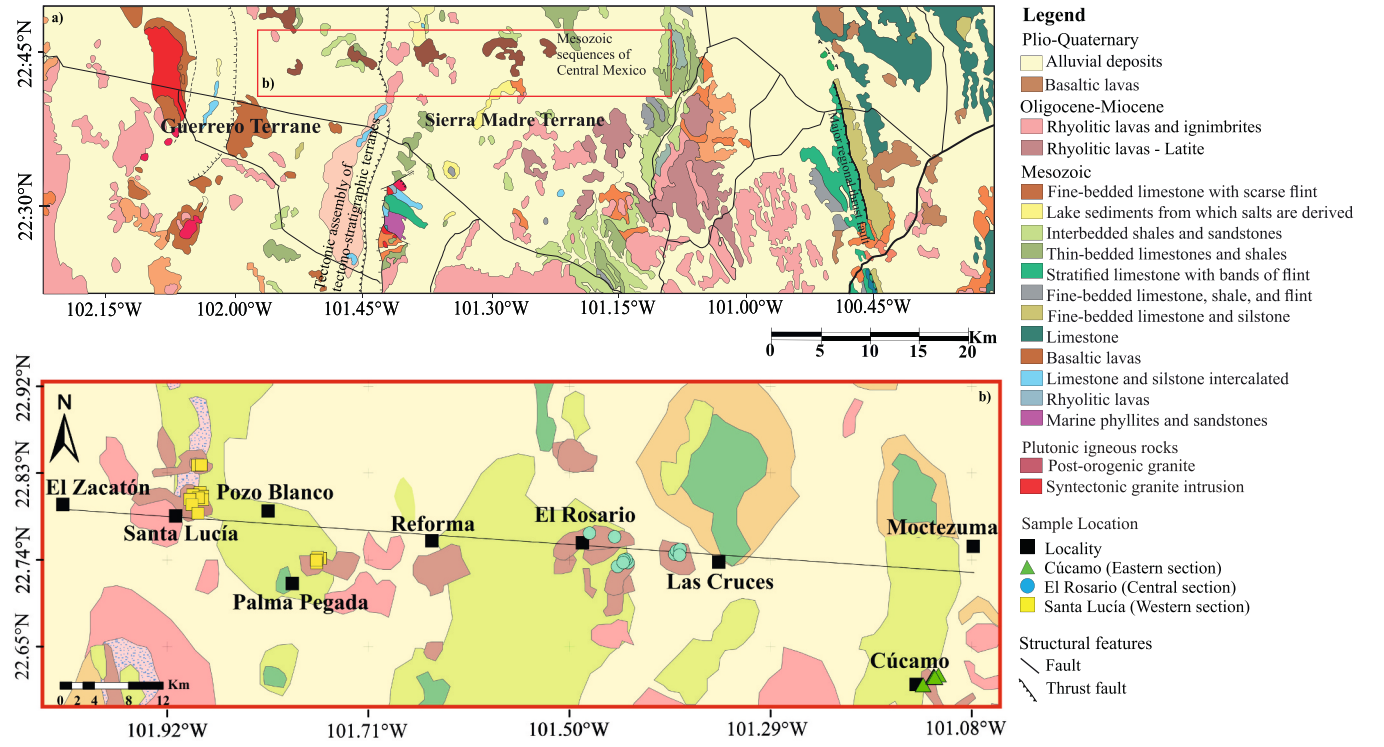

Fig. 2. a) Regional map of the Ventura Espiritu Santo Volcanic Field (VESVF), based on and modified from the 1:250,000 San Luis Potosí (F14-4) and Zacatecas (F13-6) mining geological maps; b) Geologic map shows the Plio-Quaternary mafic volcanic rocks from the Ventura Espiritu Santo Volcanic Field (VESVF) between the localities of Cúcamo and Santa Lucía. Sample locations are indicates as follow: green triangles for Cúcamo basalt (eastern section), blue circles for El Rosario basalt (central section) and yellow squares for Santa Lucia basalt (western section). (For interpretation of the references to color in this figure legend, the reader is referred to the web version of this article.)

1989, 1995a; Paz-Moreno et al., 2003; Aranda-Gómez et al., 2005; Dávalos-Elizondo et al., 2016). Between Cúcamo and El Zacatón, several key localities, including El Rosario and Santa Lucía, were selected for fieldwork and sample collection for the present study.

2.1. Stratigraphy and field relationships

The VESVF stratigraphy extends from the Mesozoic metamorphic basement to the Plio-Quaternary mafic volcanic rocks in the Central Mexico Basin (Fig. 3). Above the basement lies a polymictic conglomerate, deposited during the Paleocene–Eocene (Labarthe–Hernández et al., 1982). This is overlain by a volcanic sequence comprising rhyolites, rhyolitic tuffs, and explosive breccias (Fig. 3), which are associated with the Upper Oligocene Panalillo rhyolite of the San Luis Potosi Volcanic Field (SLPVF), dated at ~26 Ma (Labarthe–Hernández et al., 1982).

The lithology studied within the VESVF consists of Plio-Quaternary mafic rocks exposed between the localities of Cúcamo and Santa Lucía. The lava outcrops are grouped into three units distinguished in the field by their characteristics (Unit A, B and C; Fig. 3). At the Cúcamo and El Rosario localities, Units A and B are predominant, represented by basaltic lavas with olivine and sparse vesicle. In contrast, the Santa Lucía locality is characterized by a basaltic lava unit containing olivine nodules and minor amphibole (Unit A). Notably, peridotite xenolith occurs within Units B and C. These rocks are found as isolated lava flows, cinder and scoria cones. These units are alkaline and subalkaline in composition and are correlated with the Las Joyas Formation (Labarthe–Hernández et al., 1982), which includes basaltic lava flows, cinder cones, and basaltic tuffs. Some of these lavas contain peridotite xenoliths (Fig. 4). The mafic lavas are typically associated with the formation of cinder cones, such as those at Cerro El Toro, El Tezontle, and San Cayetano, located between the aforementioned localities. In addition, a pyroclastic deposit known as Pómez El Desierto has been documented in the area. It was originally reported by Labarthe–Hernández et al. (1982) and later interpreted by Del Pilar-Martínez et al. (2021) as being derived from a caldera located within the Trans-Mexican Volcanic Belt.

3. Sampling and analytical methods

A total thirty-four representative mafic volcanic rock samples were collected from the Cúcamo–Santa Lucía area, including nine basalts from Cúcamo, eleven from El Rosario, and fourteen from Santa Lucia for mineralogical and geochemical analysis. Of these, six samples were selected for Sr-Nd isotopic analysis. Out of thirty-four samples, nine were selected for petrographic analysis (Table 1). The sample locations and geographic coordinates are shown in Table 2. In addition, Fig. 3 shows the stratigraphic relationships where samples were collected.

3.1. Petrography

The preparation of thin sections was carried out in the petrography laboratory of the División de Geociencias Aplicadas, Instituto Potosino de Investigación Científica y Tecnológica (IPICYT), San Luis Potosí, Mexico. The texture and modal compositions were obtained by point counting on thin sections using a Leica petrographic microscope and a Pelcon manual counter. Approximately nine hundred points were made per sample (Table 1).

3.2. Whole rock geochemistry

The thirty-four samples were prepared at the IPICYT for whole-rock geochemical analysis (Table 2). Major elements concentrations were performed by X-ray Fluorescence (WDXRF) spectrometer, Rigaku ZSX

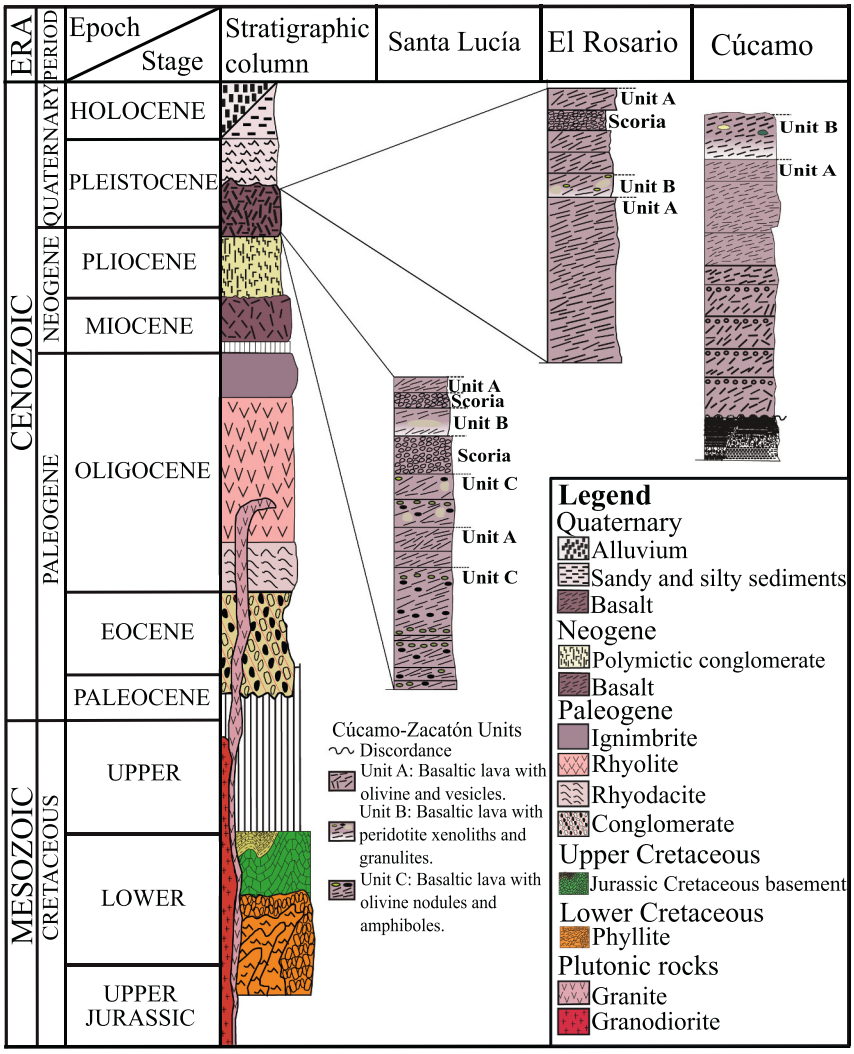

Fig. 3. Stratigraphic column of the VESVF between the localities of Cúcamo and Santa Lucía.

Primus II model Wavelength Dispersive, rhodium X-ray tube, 4 kW power at IPICYT. The analytical procedures were given by Verma et al. (2018, 2019). The samples preparation for trace and rare earth elements was carried out by total digestions at the Instituto de Investigación de Zonas Desérticas, Universidad Autónoma de San Luis Potosí, San Luis Potosí and analyses were performed at Universidad de Centro de México (UCEM), San Luis Potosí, Mexico by Inductive Coupled Plasma-Mass Spectrometry (ICP-MS) using Thermo Scientific, model iCAP-RQ. Powdered rock samples were subjected to a total digestion protocol prior to geochemical analysis. The procedure was as follows: (i) 0.1 g of finely ground powdered rock sample was weighed into digestion vessels; (ii) each sample was spiked with 500 μL of an internal iridium (Ir) tracer solution at a concentration of 25 μg/mL; (iii) 15 mL of 48 % HF (analytical grade) was added to each sample, which was then placed on a hotplate and evaporated to near dryness, reducing the volume to approximately 1 mL; (iv) subsequently, 15 mL of ultrapure (or distilled) 10 % HNO_3 was added, and the solution was again evaporated to ~1 mL; (v) finally, 10 mL of HCl were added and evaporated until no precipitate remained. The resulting solution was brought to a final volume of 50 mL using 2 % HNO_3 and transferred to Falcon tubes for analysis.

Reagent blanks were processed using the above-mentioned procedure to ensure quality control. Analytical accuracy and precision were monitored following the protocols established by Verma et al. (2023) and Shukla et al. (2024).

3.3. Whole rock Sr-Nd isotopic analysis

A total of six samples were selected for Sr-Nd isotopic analyses, which were carried out at the Geochronology Unit of the Complutense University of Madrid, Spain. Sr-Nd analyzes were performed on whole rock using isotope dilution thermal ionization mass spectrometry (ID-TIMS; Phoenix-IsotopX). Basalt sample preparation begins by weighing 0.1 g in pre-cleaned Teflon® digestion vessels and dissolved in a mixture of 4 mL 40 % HF and 2 mL 65 % HNO_3 (Merck-Suprapur®). Samples were placed in the oven at 120 °C for 3 days. The solutions were dried on a hot plate at 120 °C and 1 mL of 65 % HNO_3 was added for a maximum evaporation of the SiF_4. Then, 4 mL of distilled 6 M HCl were added to the samples and returned to the oven at 120 °C for 24 h. Once again, the samples are brought to 120 °C to later reconstruct with 3 mL of 2.5 M HCl (distilled and titrated). The final solutions were taken to a double-step chromatographic separation: i) by using DOWEX AG®50 × 8 200–400 mesh cation exchange resin (Bio-Rad Laboratories, Inc., USA) to separate the Sr fraction (without Rb) and the rare earth elements (REE) from the matrix of the sample bulk, and ii) LnResin® extraction resin (50–100 μm) (Eichrom Technologies, Lisle, IL, USA) was used to separate Nd from interfering Sm isotopes. In this last step, Nd (using 0.3 N HCl as eluent) and Sm (using 0.4 N HCl as eluent) fractions of the samples are completely separated.

Sr fractions were loaded, along with 2 μL of ultrapure 1 M H_3PO_4 and 2 μL of Ta_2O_5, in a Re ribbon previously degassed. They were analyzed

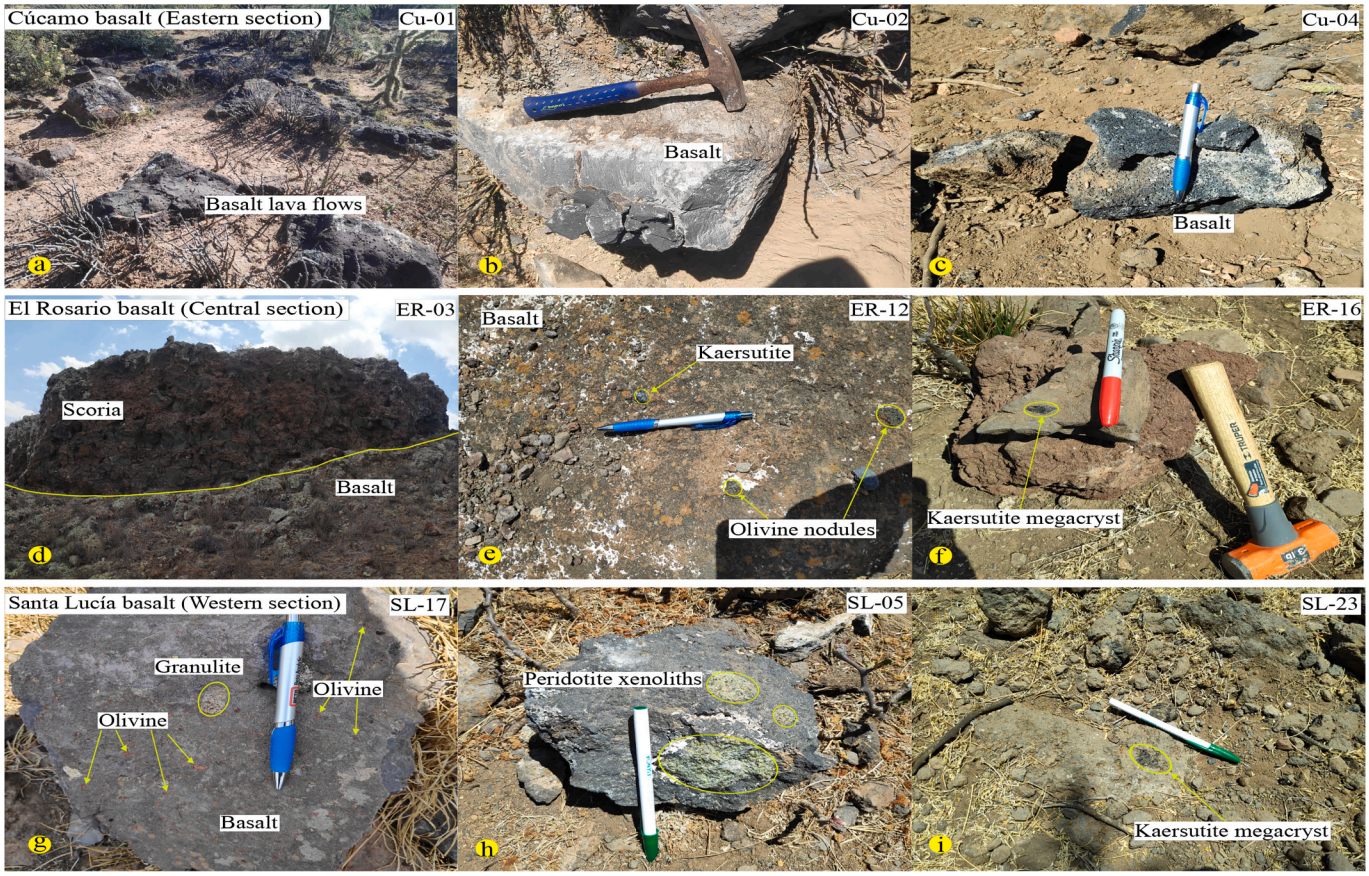

Fig. 4. Representative field photographs of the Cúcamo–Santa Lucía, VESVF. Cúcamo basalt (eastern section): a) associated lavas flow, b) basaltic sample (Cu-02) collected for geochemical analysis, and c) basaltic sample with vesicles. El Rosario basalt (central section): d) contact between the Jurassic-Cretaceous basement, Plio-Quaternary basalt and a scoria wall, e) 2.6 cm long olivine nodules and 1.5 cm long kaersutite megacrystals are observed embedded in basalt, f) 2.5 cm kaersutite megacrystal embedded in hand sample. Santa Lucía basalt (western section): g) basalt with nodules of altered olivine and granulite, h) peridotite xenoliths and i) 2.8 cm altered kaersutite megacrystal embedded in basaltic lava.

Table 1
Petrographic information of mafic rocks in thin section from VESVF.

Sample	Rock type	Locality	Lat (N)°	Long (W)°	Pl	Ol	Px	Amph	Idg	Op	Vesicles
Cu-03	Basanite	Cúcamo	22.615049	101.118927	57	20	4	1	–	11	4
Cu-05	Basanite	Cúcamo	22.614549	101.118501	60	19	3	–	–	7	5
Cu-08	Basanite	Cúcamo	22.615931	101.119826	57	17	5	–	1	8	5
ER-05	Trachybasalt	El Rosario	22.747036	101.389843	60	18	4	–	10	3	2
ER-16	Trachybasalt	El Rosario	22.738018	101.442838	62	14	3	–	8	4	4
ER-17	Trachybasalt	El Rosario	22.730758	101.451829	53	20	7	–	3	2	5
ST-11	Basalt	Santa Lucía	22.808271	101.890576	57	7	3	1	4	17	7
ST-12	Basanite	Santa Lucía	22.737347	101.768381	54	8	4	1	5	20	8
ST-24	Trachybasalt	Santa Lucía	22.739156	101.763971	53	13	7	1	4	18	4

The modal composition is presented in percentage (%). Abbreviations: Ol = olivine, Px = pyroxene (ortho-Opx and clino-Cpx), Pl = plagioclase, Amph = Amphibole, Idg = Iddingsite and Op: opaque minerals.

following a multi-dynamic collection method, always maintaining a stable ion beam intensity of 3 V in mass ^{88}Sr for a maximum of 160 replicas. $^{87}Sr/^{86}Sr$ isotope ratios were corrected for possible ^{87}Rb interferences and potential fractionation was normalized to the $^{86}Sr/^{88}Sr$ ratio of 0.1194 (Nier, 1938). Final Sr isotope ratios of the samples were in turn corrected considering the analyzed Sr-isotope standard NBS 987 that yields an average value of 0.710248 for 9 replicates with an internal precision of 0.00002 (2SD). Nd (Sm-free) fractions were loaded, together with 2 μL of ultrapure 0.05 M H_3PO_4, on a lateral pre-cleaned Re ribbon in a triple Re-ribbon arrangement. They were also analyzed by using a multi-dynamic collection method. For this purpose, ^{144}Nd ion beam was kept stable at 1 V intensity during a maximum of 160 replicas. A normalized value of 0.7219 for the $^{146}Nd/^{144}Nd$ ratio (O'Nions et al., 1979) was considered for a continuous correction of the Nd-isotope fractionation. Absence of ^{142}Ce and ^{144}Sm isobaric interferences were continuously checked and corrected during the Nd isotope analysis. Nd-reference standard JNdi-1 (Tanaka et al., 2000) was used for a final correction of the resulting $^{143}Nd/^{144}Nd$ isotope ratios, obtaining an average value of $^{143}Nd/^{144}Nd = 0.512101$ for 10 replicas with an internal precision of 0.000007 (2SD). Likewise, Sm fractions were also dissolved in 2 μL of ultrapure 0.05 M H_3PO_4 and loaded on a lateral Re filament in a triple filament disposition. Sm analysis was carried out following a static multicollection method, keeping a 1 V stable intensity of the ^{149}Sm mass ion beam during 100 replicas. Analytical errors for $^{87}Sr/^{86}Sr$, $^{147}Sm/^{144}Nd$, and $^{143}Nd/^{144}Nd$ ratios were estimated in 0.01 %, 0.1 %, and 0.006 %, respectively. Total Sr and Nd procedural blank

Table 2
Major, trace and rare earth elements geochemistry of mafic rocks from the Ventura Espiritu Santo Volcanic Field (VESVF), San Luis Potosi, Mexico (major element in weight percent (also known as % m/m) and trace and rare earth elements in μg/g).

Sample	Cu-01	Cu-02	Cu-03	Cu-04	Cu-05	Cu-06	Cu-07
Rock (TAS)	Basanite	Trachybasalt	Basanite	Trachybasalt	Basanite	Basanite	Trachybasalt
Locality	Cúcamo	Cúcamo	Cúcamo	Cúcamo	Cúcamo	Cúcamo	Cúcamo
Long. (°W)	101.119325	101.114715	101.118927	101.118464	101.118501	101.119642	101.119413
Lat. (°N)	22.614963	22.616902	22.615049	22.613990	22.614549	22.614688	22.615630
SiO_2	45.44	47.49	44.97	44.54	44.15	45.78	45.71
TiO_2	1.84	1.87	1.61	1.59	1.95	1.98	1.54
Al_2O_3	14.47	13.68	16.13	15.67	13.33	14.43	13.97
$Fe_2O_3^t$	11.40	12.52	8.52	9.26	12.57	11.79	11.90
MnO	0.22	0.21	0.17	0.17	0.19	0.18	0.15
MgO	7.68	6.92	7.49	7.36	6.97	6.91	7.32
CaO	9.53	8.36	10.43	10.31	10.50	9.35	10.59
Na_2O	2.81	2.25	2.77	2.13	2.92	3.03	2.33
K_2O	3.56	3.45	3.63	3.27	2.86	3.91	3.24
P_2O_5	2.10	1.88	2.22	2.08	2.10	2.09	2.04
LOI	1.34	1.23	1.66	2.93	1.8	0.75	1.54
Sum	100.41	99.87	99.60	99.33	99.39	100.21	100.35
Adjusted							
$(SiO_2)_{adj}$	46.29	48.63	46.24	46.56	45.76	46.46	46.71
$(TiO_2)_{adj}$	1.88	1.91	1.66	1.66	2.02	2.01	1.58
$(Al_2O_3)_{adj}$	14.74	14.01	16.58	16.38	13.81	14.65	14.28
$(Fe_2O_3^t)_{adj}$	2.47	2.73	1.86	2.06	1.99	2.54	2.58
$(MnO)_{adj}$	8.23	9.09	6.21	6.86	9.93	8.48	8.61
$(MgO)_{adj}$	0.22	0.22	0.17	0.18	0.20	0.19	0.16
$(CaO)_{adj}$	7.82	7.09	7.70	7.69	7.23	7.02	7.48
$(Na_2O)_{adj}$	9.71	8.57	10.72	10.77	10.88	9.49	10.82
$(K_2O)_{adj}$	2.87	2.31	2.84	2.23	3.02	3.07	2.38
$(P_2O_5)_{adj}$	3.63	3.53	3.74	3.42	2.97	3.97	3.31
Sum	100	100	100	100	100	100	100
Q	–	–	–	–	–	–	–
Or	21.45	20.88	22.07	20.23	17.54	23.44	19.59
Ab	12.61	19.50	9.33	13.32	12.04	11.75	13.68
An	16.63	17.44	21.44	24.57	15.35	14.45	18.46
Ne	6.31	–	7.99	3.00	7.34	7.72	3.52
C	–	–	–	–	–	–	–
Di-Mg*	6.31	6.49	10.12	8.53	12.05	10.01	11.47
Di-Fe*	4.51	3.74	3.42	3.30	7.95	5.24	6.10
Hy-Mg*	–	4.81	–	–	–	–	–
Hy-Fe+	–	3.18	–	–	–	–	–
Mt	3.58	3.95	2.70	2.98	2.88	3.69	3.75
IL	3.56	3.63	3.14	3.15	3.84	3.81	3.00
Ap	4.97	4.44	5.28	5.04	5.05	4.92	4.83
Mg#	57.16	52.27	63.52	61.14	52.36	53.75	54.94
FeOt/MgO	1.33	1.63	1.02	1.13	1.62	1.53	1.46
Ba	99.75	88.77	101.02	73.32	65.44	57.05	51.80
Co	19.01	10.89	9.28	6.86	5.70	4.54	4.79
Cr	141.29	60.93	56.07	40.68	35.30	26.52	21.73
Cs	0.17	0.20	0.16	0.12	0.11	0.10	0.10
Cu	7.85	5.44	4.31	4.24	3.71	3.00	2.48
Ga	10.81	8.24	6.09	4.80	3.87	3.13	2.62
Hf	0.97	1.12	1.17	1.22	1.17	1.17	1.17
Nb	32.35	27.60	22.74	18.89	15.79	13.49	11.15
Ni	65.64	29.10	30.08	19.54	18.49	14.58	12.10
Pb	0.56	0.75	0.65	0.69	0.71	0.69	0.71
Rb	14.08	12.82	9.051	6.98	5.66	4.92	4.37
Sc	7.62	4.39	3.03	2.45	1.78	1.29	1.09
Sr	389.32	313.27	263.65	207.19	175.94	150.27	132.05
Ta	1.54	0.88	0.72	0.89	0.72	0.72	0.76
Th	1.04	0.89	0.87	0.93	0.89	0.92	0.96
U	0.45	0.54	0.56	0.58	0.59	0.61	0.63
V	70.33	39.77	29.63	23.22	18.17	13.57	11.06
Y	7.96	7.003	5.49	4.94	4.53	4.52	3.97
Zn	35.20	25.37	20.12	14.45	12.16	9.76	8.07
Zr	105.02	92.81	74.20	62.09	49.33	41.79	36.63
La	13.09	13.74	12.39	11.80	10.46	9.58	8.84
Ce	26.83	27.64	25.26	23.78	21.41	19.53	17.88
Pr	2.91	3.11	2.88	2.77	2.50	2.29	2.11
Nd	12.15	11.47	10.86	10.60	9.67	9.00	8.40
Sm	2.26	2.43	2.34	2.29	2.11	1.97	1.85
Eu	0.73	0.77	0.76	0.75	0.70	0.66	0.62
Gd	1.77	1.86	1.78	1.78	1.63	1.54	1.48
Tb	0.22	0.23	0.23	0.23	0.21	0.20	0.20

(*continued on next page*)

Table 2 (*continued*)

Sample	Cu-01	Cu-02	Cu-03	Cu-04	Cu-05	Cu-06	Cu-07
Rock (TAS)	Basanite	Trachybasalt	Basanite	Trachybasalt	Basanite	Basanite	Trachybasalt
Locality	Cúcamo	Cúcamo	Cúcamo	Cúcamo	Cúcamo	Cúcamo	Cúcamo
Long. (°W)	101.119325	101.114715	101.118927	101.118464	101.118501	101.119642	101.119413
Lat. (°N)	22.614963	22.616902	22.615049	22.613990	22.614549	22.614688	22.615630
Dy	1.006	1.09	1.07	1.11	1.02	0.99	0.96
Ho	0.17	0.19	0.18	0.19	0.18	0.17	0.16
Er	0.42	0.47	0.45	0.48	0.44	0.42	0.41
Tm	0.05	0.055	0.05	0.056	0.052	0.05	0.050
Yb	0.30	0.33	0.32	0.34	0.32	0.31	0.30
Lu	0.04	0.04	0.04	0.04	0.04	0.04	0.04
TREE	60.95	62.36	57.56	55.13	49.74	45.79	42.37
$(La/Yb)_{CN}$	29.52	27.84	26.05	23.22	22.19	21.006	19.72
$(La/Sm)_{CN}$	3.61	3.53	3.30	3.21	3.09	3.04	2.97
$(La/Yb)_{PM}$	29.57	27.89	26.10	23.26	22.24	21.04	19.75
$(La/Sm)_{PM}$	3.62	3.54	3.31	3.22	3.10	3.05	2.98
$(Gd/Yb)_{PM}$	4.74	4.49	4.46	4.18	4.11	4.03	3.94
(Eu/Eu*)	1.07	1.07	1.10	1.09	1.11	1.11	1.11
(Nb/Nb*)	0.71	0.62	0.49	0.44	0.42	0.27	0.27
(Ti/Ti*)	2.63	2.65	2.44	2.54	3.32	3.45	2.92
(Ta/Ta*)	2.35	1.37	1.13	1.64	1.50	1.67	1.91

Sample	Cu-08	Cu-09	ER-03	ER-04	ER-05	ER-08	ER-09
Rock (TAS)	Basanite	Basanite	Basalt	Basalt	Trachybasalt	Trachybasalt	Basanite
Locality	Cúcamo	Cúcamo	El Rosario	El Rosario	El Rosario	El Rosario	El Rosario
Long. (°W)	101.119826	101.130828	101.385588	101.386151	101.389843	101.391826	101.481383
Lat. (°N)	22.615931	22.606585	22.743588	22.748536	22.747036	22.743512	22.765654
SiO_2	46.17	45.96	42.82	46.60	46.66	44.57	44.52
TiO_2	1.90	2.06	2.10	1.51	1.718	2.07	2.18
Al_2O_3	14.09	15.06	16.81	17.53	16.11	13.24	14.34
$Fe_2O_3^t$	11.43	12.31	13.87	11.34	11.31	14.98	14.21
MnO	0.17	0.17	0.15	0.15	0.15	0.15	0.19
MgO	7.22	7.02	5.03	6.40	6.98	7.19	7.02
CaO	8.57	8.52	7.52	8.08	7.67	7.51	7.88
Na_2O	2.83	3.69	1.58	3.03	3.38	3.11	3.70
K_2O	3.90	3.05	1.79	1.40	1.51	1.68	3.04
P_2O_5	2.00	2.03	1.16	1.51	1.46	1.35	1.93
LOI	1.52	0.09	6.09	2.46	2.18	3.51	0.97
Sum	99.85	100.00	98.93	100.02	99.15	99.38	100.03
Adjusted							
$(SiO_2)_{adj}$	47.39	46.46	46.72	48.24	48.56	47.08	45.46
$(TiO_2)_{adj}$	1.95	2.09	2.30	1.57	1.79	2.19	2.23
$(Al_2O_3)_{adj}$	14.47	15.22	18.34	18.15	16.77	13.99	14.65
$(Fe_2O_3^t)_{adj}$	2.49	2.64	2.31	1.79	2.50	3.36	3.09
$(MnO)_{adj}$	8.32	8.82	11.54	8.95	8.34	11.21	10.28
$(MgO)_{adj}$	0.18	0.17	0.16	0.15	0.16	0.16	0.19
$(CaO)_{adj}$	7.42	7.10	5.49	6.63	7.26	7.59	7.18
$(Na_2O)_{adj}$	8.80	8.61	8.21	8.37	7.99	7.93	8.05
$(K_2O)_{adj}$	2.91	3.73	1.72	3.14	3.53	3.29	3.78
$(P_2O_5)_{adj}$	4.01	3.09	1.96	1.45	1.57	1.78	3.11
Sum	100	100	100	100	100	100	100
Q	–	–	–	–	–	–	–
Or	23.69	18.26	11.56	8.56	9.30	10.49	18.39
Ab	15.62	18.42	14.59	26.55	29.85	27.82	16.70
An	14.57	15.66	32.45	31.16	25.28	18.17	13.79
Ne	4.89	7.12	0	0	0	0	8.30
C	–	–	1.49	0	0	0	0
Di-Mg*	8.55	7.23	0	0.07	2.37	5.83	6.63
Di-Fe*	4.16	3.88	0	0.05	1.21	3.90	4.21
Hy-Mg*	–	–	13.33	6.58	4.27	1.070	0
Hy-Fe*	–	–	15.38	5.04	2.50	0.82	0
Mt	3.61	3.83	3.34	2.59	3.62	4.87	4.47
IL	3.70	3.96	4.36	2.98	3.39	4.16	4.23
Ap	4.76	4.76	2.92	3.62	3.52	3.30	4.58
Mg#	55.59	53.07	41.83	52.79	55.00	48.73	49.48
FeO^t/MgO	1.42	1.57	2.47	1.59	1.45	1.87	1.82
Ba	50.71	50.23	46.21	40.38	39.93	88.96	82.39
Co	4.92	4.29	3.20	3.17	3.12	7.99	9.08
Cr	19.30	19.69	13.79	17.99	19.74	25.39	19.11
Cs	0.09	0.10	0.10	0.09	0.09	0.02	0.02

(*continued on next page*)

Table 2 (*continued*)

Sample	Cu-08	Cu-09	ER-03	ER-04	ER-05	ER-08	ER-09
Rock (TAS)	Basanite	Basanite	Basalt	Basalt	Trachybasalt	Trachybasalt	Basanite
Locality	Cúcamo	Cúcamo	El Rosario	El Rosario	El Rosario	El Rosario	El Rosario
Long. (°W)	101.119826	101.130828	101.385588	101.386151	101.389843	101.391826	101.481383
Lat. (°N)	22.615931	22.606585	22.743588	22.748536	22.747036	22.743512	22.765654
Cu	2.10	2.05	1.03	1.55	2.44	6.53	7.35
Ga	2.46	2.25	1.94	1.90	1.88	5.07	7.05
Hf	1.16	1.11	0.99	0.93	0.94	1.24	1.7489712
Nb	11.24	10.68	7.85	7.50	7.46	17.54	29.57
Ni	13.91	14.47	7.08	9.31	8.82	37.18	12.59
Pb	0.73	0.74	0.34	0.17	0.28	−0.12	0.23
Rb	4.26	5.76	3.46	2.28	2.36	4.50	6.40
Sc	0.98	0.85	0.76	0.78	0.78	2.39	3.35
Sr	124.18	120.62	103.29	94.51	92.41	96.68	133.46
Ta	0.82	0.93	0.71	0.66	0.66	1.39	2.20
Th	0.99	1.02	1.08	1.09	1.08	0.67	1.23
U	0.64	0.59	0.45	0.45	0.45	0.41	0.61
V	12.24	13.48	10.83	11.22	11.64	39.40	45.29
Y	3.77	3.48	2.91	2.79	2.80	3.59	5.97
Zn	7.63	6.41	4.15	3.59	3.53	22.86	30.18
Zr	34.87	32.45	27.20	26.07	26.57	42.15	57.17
La	8.66	8.29	6.21	5.95	5.92	7.04	9.25
Ce	17.72	16.89	12.76	11.95	11.85	12.23	19.06
Pr	2.08	1.96	2.14	1.99	1.90	2.27	3.52
Nd	8.24	10.04	8.55	7.83	7.75	7.55	11.75
Sm	1.81	1.70	1.36	1.25	1.24	1.71	2.60
Eu	0.62	0.58	0.48	0.44	0.43	0.51	0.79
Gd	1.45	1.37	1.15	1.07	1.08	1.40	2.15
Tb	0.19	0.18	0.15	0.14	0.14	0.17	0.27
Dy	0.94	0.90	0.76	0.72	0.72	0.91	1.39
Ho	0.16	0.15	0.13	0.13	0.13	0.14	0.22
Er	0.40	0.39	0.34	0.34	0.34	0.37	0.58
Tm	0.04	0.04	0.04	0.04	0.04	0.03	0.05
Yb	0.30	0.30	0.27	0.27	0.27	0.26	0.41
Lu	0.04	0.04	0.03	0.03	0.03	0.01	0.04
TREE	41.75	41.96	33.64	31.45	31.18	33.72	50.71
$(La/Yb)_{CN}$	19.55	18.91	15.50	14.58	14.39	18.50	15.30
$(La/Sm)_{CN}$	2.97	3.04	2.85	2.98	2.98	2.57	2.22
$(La/Yb)_{PM}$	19.59	18.94	15.52	14.60	14.41	18.53	15.33
$(La/Sm)_{PM}$	2.99	3.06	2.85	3.00	2.99	2.58	2.23
$(Gd/Yb)_{PM}$	3.90	3.73	3.42	3.11	3.12	4.39	4.24
(Eu/Eu*)	1.13	1.13	1.17	1.16	1.15	1.02	1.02
(Nb/Nb*)	0.22	0.27	0.29	0.35	0.33	0.76	0.72
(Ti/Ti*)	3.66	4.19	5.6	4.14	4.75	4.83	3.16
(Ta/Ta*)	2.12	2.46	2.32	2.33	2.35	3.10	4.45
Sample	ER-14	ER-15	ER-16	ER-17	ER-18	ER-19	ST-01
Rock (TAS)	Basanite	Basalt	Basalt	Trachybasalt	Trachybasalt	Trachybasalt	Trachybasalt
Locality	El Rosario	El Rosario	El Rosario	El Rosario	El Rosario	El Rosario	Santa Lucía
Long. (°W)	101.454980	101.445982	101.445365	101.442838	101.441039	101.451829	101.889374
Lat. (°N)	22.761693	22.734747	22.737258	22.738018	22.734805	22.730758	22.837130
SiO_2	44.08	46.80	46.88	47.45	42.82	46.60	46.65
TiO_2	1.11	1.65	1.23	2.10	2.10	1.51	1.72
Al_2O_3	18.70	16.15	16.61	15.35	16.81	17.53	16.11
$Fe_2O_3^t$	12.21	11.984	11.14	12.51	13.87	11.34	11.31
MnO	0.058	0.14	0.12	0.18	0.14	0.14	0.15
MgO	5.96	6.97	7.21	6.99	5.03	6.40	6.98
CaO	8.38	7.76	8.31	8.18	7.52	8.08	7.67
Na_2O	2.79	2.88	2.57	3.42	1.58	3.03	3.39
K_2O	3.81	0.95	1.43	1.99	1.79	1.40	1.51
P_2O_5	1.98	1.61	1.61	1.78	1.15	1.50	1.46
LOI	1.24	2.24	3.36	−0.59	6.09	2.46	2.18
Sum	100.35	99.17	100.51	99.38	99.42	100.27	99.68
Adjusted							
$(SiO_2)_{adj}$	44.92	48.80	48.73	47.94	45.99	46.35	46.94
$(TiO_2)_{adj}$	1.14	1.72	1.28	2.12	1.50	2.14	1.40
$(Al_2O_3)_{adj}$	19.05	16.84	17.27	15.51	15.48	15.05	19.74
$(Fe_2O_3^t)_{adj}$	2.65	1.91	1.77	2.69	2.76	3.17	2.18
$(MnO)_{adj}$	8.82	9.53	8.84	8.96	9.21	10.56	7.28
$(MgO)_{adj}$	0.06	0.15	0.13	0.18	0.16	0.17	0.08
$(CaO)_{adj}$	6.07	7.27	7.50	7.07	7.46	7.19	5.20
$(Na_2O)_{adj}$	8.54	8.10	8.64	8.27	10.67	8.51	9.77

(*continued on next page*)

Table 2 (*continued*)

Sample	ER-14	ER-15	ER-16	ER-17	ER-18	ER-19	ST-01
Rock (TAS)	Basanite	Basalt	Basalt	Trachybasalt	Trachybasalt	Trachybasalt	Trachybasalt
Locality	El Rosario	El Rosario	El Rosario	El Rosario	El Rosario	El Rosario	Santa Lucía
Long. (°W)	101.454980	101.445982	101.445365	101.442838	101.441039	101.451829	101.889374
Lat. (°N)	22.761693	22.734747	22.737258	22.738018	22.734805	22.730758	22.837130
$(K_2O)_{adj}$	2.84	3.00	2.68	3.46	1.43	2.65	2.98
$(P_2O_5)_{adj}$	3.89	0.99	1.49	2.01	3.61	2.58	2.61
Sum	100	100	100	100	100	100	100
Q	–	–	–	–	–	–	–
Or	22.99	5.85	8.81	11.87	11.56	8.56	9.30
Ab	10.39	25.41	22.64	29.27	14.59	26.55	29.84
An	27.73	29.19	30.71	20.84	32.45	31.16	25.28
Ne	7.40	0	0	0	0.88	0	2.15
C	0	0.12	0	0	1.49	0	0
Di-Mg*	0.69	0	0.62	4.42	8.47	4.94	1.94
Di-Fe*	0.49	0	0.37	2.42	4.94	3.26	1.23
Hy-Mg*	0	13.84	11.55	1.40	13.33	6.58	4.27
Hy-Fe*	0	10.21	7.97	0.88	15.38	5.04	2.50
Mt	3.83	2.76	2.56	3.90	3.34	2.59	3.62
IL	2.16	3.27	2.43	4.02	4.36	2.98	3.39
Ap	4.69	3.89	3.87	4.17	2.93	3.62	3.52
Mg#	49.14	53.55	56.19	52.55	53.20	48.86	50.06
FeO^t/MgO	1.84	1.54	1.39	1.60	2.47	1.59	1.45
Ba	678.22	491.76	191.29	196.55	46.21	40.38	39.93
Co	47.26	52.82	17.95	16.11	3.21	3.17	3.12
Cr	93.11	323.18	82.65	87.34	13.79	17.98	19.73
Cs	0.66	1.48	0.46	0.31	0.10	0.09	0.09
Cu	35.26	24.31	11.46	10.02	1.03	1.55	2.44
Ga	35.92	27.97	10.79	10.86	1.94	1.90	1.88
Hf	7.74	7.38	2.86	3.12	0.99	0.93	0.95
Nb	134.75	104.10	38.52	40.06	7.85	7.50	7.47
Ni	67.96	360.94	78.93	69.87	7.08	9.31	8.82
Pb	3.74	3.21	1.85	1.67	0.35	0.17	0.28
Rb	51.40	44.19	14.12	16.50	3.46	2.28	2.37
Sc	22.53	19.88	7.21	7.13	0.76	0.78	0.78
Sr	2047.10	1210.91	470.75	467.95	103.29	94.52	92.41
Ta	9.76	7.94	2.96	3.20	0.71	0.66	0.66
Th	6.99	6.48	2.55	2.81	1.08	1.10	1.08
U	2.27	2.23	0.92	0.96	0.46	0.46	0.45
V	228.05	202.72	78.76	72.02	10.83	11.22	11.64
Y	36.52	28.05	10.74	11.23	2.91	2.80	2.80
Zn	178.43	312.93	46.83	43.46	4.15	3.59	3.53
Zr	427.10	337.57	130.06	137.43	27.20	26.07	26.57
La	68.73	55.81	21.84	23.07	6.21	5.95	5.92
Ce	137.37	111.60	43.24	45.80	12.76	11.95	11.85
Pr	16.37	13.41	5.16	5.48	2.14	2.00	1.90
Nd	63.59	52.76	20.35	21.69	8.59	7.83	7.75
Sm	12.33	10.38	4.03	4.27	1.36	1.25	1.24
Eu	3.91	3.35	1.29	1.37	0.48	0.44	0.43
Gd	9.64	8.43	3.23	3.49	1.15	1.06	1.08
Tb	1.40	1.22	0.47	0.51	0.15	0.14	0.14
Dy	6.91	6.16	2.40	2.57	0.76	0.72	0.72
Ho	1.20	1.10	0.42	0.45	0.13	0.13	0.13
Er	3.03	2.79	1.07	1.14	0.34	0.34	0.34
Tm	0.39	0.36	0.14	0.15	0.04	0.04	0.04
Yb	2.29	2.14	0.82	0.86	0.27	0.28	0.28
Lu	0.33	0.32	0.13	0.13	0.04	0.04	0.04
TREE	320.60	263.68	102.19	108.40	93.15	97.15	92.44
$(La/Yb)_{CN}$	20.35	17.71	18.17	18.23	15.50	14.58	14.39
$(La/Sm)_{CN}$	3.48	3.35	3.38	3.37	2.85	2.98	2.98
$(La/Yb)_{PM}$	20.38	17.74	18.20	18.26	15.52	14.61	14.41
$(La/Sm)_{PM}$	3.49	3.36	3.39	3.38	2.86	3.00	2.99
$(Gd/Yb)_{PM}$	3.40	3.19	3.20	3.28	3.17	3.25	2.95
(Eu/Eu*)	1.10	1.10	1.09	1.08	1.17	1.16	1.15
(Nb/Nb*)	1.81	2.65	1.38	1.14	0.29	0.35	0.33
(Ti/Ti*)	0.31	0.56	1.09	1.7	1.32	1.86	1.23
(Ta/Ta*)	2.52	2.67	2.56	2.64	2.33	2.33	2.36

Sample	ST-02	ST-03	ST-14	ST-15	ST-18	ST-19	ST-21
Rock (TAS)	Basanite	Basanite	Basanite	Basalt	Basalt	Trachybasalt	Trachybasalt
Locality	Santa Lucía	Santa Lucía	Santa Lucía	Santa Lucía	Santa Lucía	Santa Lucía	Santa Lucía
Long. (°W)	101.893734	101.892948	101.899077	101.901213	101.892349	101.898288	101.887820
Lat. (°N)	22.834225	22.786440	22.795481	22.801200	22.802797	22.806064	22.800857

(*continued on next page*)

Table 2 (*continued*)

Sample	ST-02	ST-03	ST-14	ST-15	ST-18	ST-19	ST-21
Rock (TAS)	Basanite	Basanite	Basanite	Basalt	Basalt	Trachybasalt	Trachybasalt
Locality	Santa Lucía	Santa Lucía	Santa Lucía	Santa Lucía	Santa Lucía	Santa Lucía	Santa Lucía
Long. (°W)	101.893734	101.892948	101.899077	101.901213	101.892349	101.898288	101.887820
SiO_2	44.57	44.52	44.08	46.80	46.88	47.45	45.06
TiO_2	2.07	2.18	1.11	1.65	1.23	2.09	1.84
Al_2O_3	13.24	14.35	18.70	16.15	16.61	15.35	18.20
$Fe_2O_3^t$	14.97	14.22	12.21	11.98	11.15	12.51	9.93
MnO	0.15	0.19	0.06	0.14	0.12	0.18	0.15
MgO	7.18	7.02	5.96	6.97	7.22	6.99	5.36
CaO	7.50	7.88	8.38	7.77	8.31	8.18	9.99
Na_2O	3.11	3.70	2.79	2.88	2.57	3.42	1.23
K_2O	1.68	3.04	3.81	0.95	1.43	1.99	3.99
P_2O_5	1.35	1.93	1.99	1.61	1.61	1.78	1.17
LOI	3.51	0.97	1.24	2.24	3.36	−0.59	2.23
Sum	99.36	99.91	99.37	99.48	99.98	99.76	99.17
Adjusted							
$(SiO_2)_{adj}$	45.88	48.73	48.51	48.31	46.46	46.28	46.86
$(TiO_2)_{adj}$	1.76	1.78	2.11	1.39	0.63	0.48	1.92
$(Al_2O_3)_{adj}$	19.76	17.45	16.10	18.78	20.52	19.97	18.93
$(Fe_2O_3^t)_{adj}$	1.61	2.35	1.79	2.32	2.30	1.95	2.20
$(MnO)_{adj}$	8.03	7.83	8.97	7.74	7.66	9.77	7.32
$(MgO)_{adj}$	0.14	0.17	0.17	0.09	0.13	0.15	0.16
$(CaO)_{adj}$	5.68	5.51	7.18	5.43	5.86	5.81	5.57
$(Na_2O)_{adj}$	9.85	9.00	9.38	9.12	9.54	9.64	10.39
$(K_2O)_{adj}$	2.90	2.45	2.66	2.19	2.39	1.01	1.28
$(P_2O_5)_{adj}$	2.63	3.33	1.78	3.29	3.05	3.46	4.15
Sum	100	100	100	100	100	100	100
Q	–	–	–	–	–	–	–
Or	10.49	18.39	22.99	5.85	8.81	11.87	24.49
Ab	27.82	16.70	10.39	25.41	22.64	29.27	10.05
An	18.17	13.79	27.73	29.18	30.71	20.8	33.63
Ne	4.00	0	0	0	2.60	0	0.44
C	0	0	0	0.12	0	0	–
Di-Mg*	2.06	4.36	5.76	2.37	0.72	0	5.23
Di-Fe*	1.36	2.72	3.32	1.55	0.49	0	2.88
Hy-Mg*	1.07	0	0	13.84	11.54	1.40	–
Hy-Fe*	0.82	0	0	10.21	7.97	0.88	–
Mt	4.87	4.47	3.83	2.76	2.56	3.89	3.18
IL	4.16	4.23	2.16	3.27	2.43	4.02	3.64
Ap	3.30	4.57	4.68	3.89	3.88	4.17	2.82
Mg#	51.65	49.70	54.74	49.64	51.76	47.30	51.66
FeO^t/MgO	1.87	1.82	1.84	1.54	1.39	1.61	1.67
Ba	88.96	82.39	678.22	491.76	191.29	196.55	395.32
Co	7.99	9.08	47.26	52.82	17.95	16.11	22.67
Cr	25.39	19.11	93.11	323.18	82.65	87.34	69.89
Cs	0.02	0.03	0.66	1.49	0.46	0.31	0.31
Cu	6.53	7.36	35.26	24.31	11.47	10.03	15.26
Ga	5.076	7.05	35.93	27.97	10.79	10.87	10.27
Hf	1.24	1.75	7.74	7.38	2.86	3.12	3.32
Nb	17.55	29.58	134.75	104.10	38.52	40.06	41.85
Ni	37.18	12.59	67.96	360.93	78.93	69.87	84.07
Pb	−0.12	0.24	3.75	3.21	1.85	1.69	0.71
Rb	4.50	6.41	51.40	44.19	14.12	16.50	25.10
Sc	2.39	3.35	22.53	19.88	7.21	7.13	8.91
Sr	96.69	133.46	2047.10	1210.91	470.74	467.94	506.10
Ta	1.39	2.20	9.76	7.94	2.96	3.20	3.79
Th	0.67	1.23	6.99	6.48	2.55	2.81	3.11
U	0.41	0.61	2.27	2.22	0.92	0.96	1.37
V	39.40	45.30	228.05	202.72	78.76	72.02	111.26
Y	3.59	5.96	36.52	28.05	10.74	11.23	10.71
Zn	22.86	30.19	178.43	312.93	46.83	43.45	21.66
Zr	42.15	57.17	427.10	337.57	130.06	137.43	117.51
La	7.05	9.25	68.73	55.81	21.84	23.06	25.62
Ce	12.23	19.06	137.36	111.59	43.24	45.80	53.95
Pr	2.27	3.52	16.37	13.42	5.16	5.48	6.55
Nd	7.55	11.75	63.59	52.77	20.35	21.69	25.89
Sm	1.71	2.59	12.33	10.38	4.03	4.27	5.25
Eu	0.51	0.79	3.91	3.35	1.28	1.36	1.83
Gd	1.40	2.15	9.64	8.43	3.23	3.49	4.32
Tb	0.17	0.27	1.39	1.22	0.47	0.51	0.69
Dy	0.91	1.40	6.91	6.16	2.40	2.57	3.00
Ho	0.14	0.22	1.20	1.10	0.42	0.45	0.72
Er	0.37	0.58	3.03	2.79	1.07	1.14	1.51
Tm	0.03	0.06	0.39	0.36	0.13	0.14	0.18

(*continued on next page*)

Table 2 (*continued*)

Sample	ST-02	ST-03	ST-14	ST-15	ST-18	ST-19	ST-21
Rock (TAS)	Basanite	Basanite	Basanite	Basalt	Basalt	Trachybasalt	Trachybasalt
Locality	Santa Lucía	Santa Lucía	Santa Lucía	Santa Lucía	Santa Lucía	Santa Lucía	Santa Lucía
Long. (°W)	101.893734	101.892948	101.899077	101.901213	101.892349	101.898288	101.887820
Yb	0.26	0.41	2.29	2.14	0.82	0.86	1.15
Lu	0.09	0.04	0.33	0.32	0.13	0.13	0.16
TREE	90.99	65.47	151.59	149.48	146.79	143.95	127.83
$(La/Yb)_{CN}$	18.50	15.30	20.35	17.71	18.17	18.23	15.10
$(La/Sm)_{CN}$	2.57	2.22	3.48	3.35	3.38	3.37	3.04
$(La/Yb)_{PM}$	18.53	15.33	20.38	17.74	18.20	18.26	15.10
$(La/Sm)_{PM}$	2.58	2.23	3.49	3.36	3.39	3.38	3.04
$(Gd/Yb)_{PM}$	2.95	2.91	3.07	3.07	3.04	3.02	3.03
(Eu/Eu*)	1.02	1.02	1.10	1.10	1.10	1.09	1.14
(Nb/Nb*)	0.76	0.73	1.81	2.67	1.38	1.14	0.69
(Ti/Ti*)	1.56	2.2	1.08	0.72	0.33	0.26	1.23
(Ta/Ta*)	3.10	4.46	2.53	2.67	2.56	2.64	2.06

Sample	ST-22	ST-23	ST-24	ST-25	ST-26	ST-27
Rock (TAS)	Basalt	Basalt	Basanite	Trachybasalt	Trachybasalt	Trachybasalt
Locality	Santa Lucía	Santa Lucía	Santa Lucía	Santa Lucía	Santa Lucía	Santa Lucía
Long. (°W)	101.887652	101.890576	101.768381	101.767969	101.767183	101.763971
Lat. (°N)	22.804407	22.808271	22.737347	22.734294	22.740175	22.739156
SiO_2	45.43	41.50	47.18	46.79	46.57	47.50
TiO_2	1.84	1.96	1.76	1.34	2.11	1.48
Al_2O_3	17.10	16.86	18.50	19.90	15.89	18.20
$Fe_2O_3^t$	10.89	13.50	9.13	10.99	12.44	11.57
MnO	0.16	0.15	0.17	0.09	0.17	0.12
MgO	5.56	4.15	5.58	5.055	5.58	5.38
CaO	9.83	10.29	8.40	8.88	7.92	7.80
Na_2O	1.24	0.99	3.13	1.73	1.28	1.36
K_2O	2.92	1.05	3.89	3.62	3.79	3.62
P_2O_5	1.27	1.14	1.64	1.48	1.29	1.47
LOI	3.29	7.42	0.08	0.48	1.99	1.00
Sum	99.57	99.02	99.48	100.37	99.04	99.71
Adjusted						
$(SiO_2)_{adj}$	47.65	45.89	47.82	47.26	48.48	48.57
$(TiO_2)_{adj}$	1.93	2.17	1.78	1.36	2.20	1.52
$(Al_2O_3)_{adj}$	17.94	18.64	18.75	20.10	16.53	18.61
$(Fe_2O_3^t)_{adj}$	1.74	2.28	1.97	2.36	2.75	2.51
$(MnO)_{adj}$	8.71	11.38	6.56	7.86	9.18	8.38
$(MgO)_{adj}$	0.17	0.17	0.17	0.09	0.18	0.13
$(CaO)_{adj}$	5.83	4.59	5.66	5.10	5.81	5.50
$(Na_2O)_{adj}$	10.32	11.38	8.51	8.96	8.25	8.17
$(K_2O)_{adj}$	1.31	1.10	3.18	1.75	1.33	1.39
$(P_2O_5)_{adj}$	3.06	1.16	3.94	3.66	3.95	3.71
Sum	100	100	100	100	100	100
Q	–	1.48	–	–	–	–
Or	18.08	6.86	23.30	21.61	23.32	21.90
Ab	11.04	9.27	16.79	14.78	11.23	11.73
An	34.05	42.51	25.25	34.68	27.48	30.70
Ne	0	0	5.47	0	0	0
C	–	–	–	0.56	–	1.07
Di-Mg*	4.06	2.15	3.32	0	2.27	0
Di-Fe*	2.84	2.58	1.60	0	1.54	0
Hy-Mg*	8.10	10.43	–	4.00	11.26	13.36
Hy-Fe*	6.50	14.36	–	3.27	8.77	10.77
Mt	2.52	3.30	2.85	3.42	4.00	3.64
IL	3.67	4.12	3.38	2.58	4.18	2.88
Ap	3.09	2.93	3.86	3.47	3.11	3.49
Mg#	50.30	37.85	54.78	47.68	47.07	47.95
FeO^t/MgO	1.76	2.93	1.47	1.96	2.00	1.93
Ba	379.59	356.97	308.80	302.93	292.56	282.14
Co	20.88	22.36	16.83	15.11	16.18	14.51
Cr	54.34	52.79	56.93	40.85	38.15	39.44
Cs	0.27	1.86	0.29	0.22	0.21	0.18
Cu	14.55	13.79	9.58	8.01	6.24	7.37
Ga	9.33	10.30	12.14	9.96	10.66	9.98
Hf	3.09	3.79	4.92	3.65	3.87	3.73
Nb	39.29	45.38	52.13	38.79	40.89	38.88
Ni	76.02	69.44	42.38	32.06	33.47	31.56
Pb	1.02	−0.17	1.24	0.94	1.22	1.36
Rb	24.64	56.53	22.50	15.44	17.02	13.76
Sc	7.80	9.63	7.14	5.66	5.72	5.56

(*continued on next page*)

Table 2 (*continued*)

Sample	ST-22	ST-23	ST-24	ST-25	ST-26	ST-27
Rock (TAS)	Basalt	Basalt	Basanite	Trachybasalt	Trachybasalt	Trachybasalt
Locality	Santa Lucía	Santa Lucía	Santa Lucía	Santa Lucía	Santa Lucía	Santa Lucía
Long. (°W)	101.887652	101.890576	101.768381	101.767969	101.767183	101.763971
Lat. (°N)	22.804407	22.808271	22.737347	22.734294	22.740175	22.739156
Sr	477.56	606.98	613.16	490.33	490.67	481.61
Ta	3.64	4.23	5.17	3.79	4.00	3.86
Th	3.12	3.40	4.74	3.35	3.52	3.52
U	1.25	1.18	1.64	1.40	1.51	1.47
V	91.79	144.21	73.27	61.26	76.27	61.90
Y	9.96	11.95	14.51	10.91	11.42	11.45
Zn	10.51	13.88	22.59	20.83	20.61	12.32
Zr	106.44	131.96	179.57	129.35	135.21	128.48
La	24.38	28.04	35.23	25.79	26.79	27.28
Ce	51.08	59.04	70.27	52.72	54.88	53.80
Pr	6.23	7.16	8.27	6.30	6.61	6.63
Nd	24.51	28.53	32.96	25.27	26.59	26.43
Sm	4.96	5.79	6.80	5.31	5.63	5.53
Eu	1.75	1.98	2.35	1.90	2.00	1.99
Gd	4.11	4.82	5.72	4.45	4.74	4.69
Tb	0.66	0.76	0.90	0.71	0.75	0.75
Dy	2.87	3.38	4.04	3.13	3.30	3.29
Ho	0.70	0.79	0.94	0.75	0.78	0.79
Er	1.46	1.69	2.04	1.57	1.64	1.67
Tm	0.17	0.20	0.25	0.19	0.19	0.20
Yb	1.11	1.28	1.58	1.20	1.25	1.29
Lu	0.15	0.18	0.23	0.17	0.18	0.18
TREE	121.30	140.30	167.55	126.37	132.05	131.24
$(La/Yb)_{CN}$	14.86	14.82	15.13	14.51	14.48	14.29
$(La/Sm)_{CN}$	3.06	3.02	3.23	3.02	2.97	3.08
$(La/Yb)_{PM}$	14.86	14.82	15.13	14.51	14.49	14.29
$(La/Sm)_{PM}$	3.06	3.02	3.23	3.02	2.97	3.08
$(Gd/Yb)_{PM}$	2.98	3.03	2.93	2.98	3.05	2.92
(Eu/Eu*)	1.14	1.11	1.12	1.16	1.15	1.16
(Nb/Nb*)	0.81	1.62	0.80	0.69	0.68	0.67
(Ti/Ti*)	1.3	1.28	0.88	0.84	1.3	0.9
(Ta/Ta*)	2.07	2.35	2.76	2.39	2.52	2.46

Abbreviations: Di-Mg – Magnesium-rich diopside; Di-Fe – Iron-rich diopside (hedenbergite); Hy-Mg – Magnesium-rich hypersthene (enstatite), Hy-Fe – Iron-rich hypersthene (ferrosilite).

was below 0.5 and 0.1 ng, respectively.

4. Results

According to the field and petrographic features observed in the northwestern part of the VESVF, the mafic volcanic rocks can be classified into three groups: the Cúcamo basalt (Eastern section; Fig. 4a–c), the El Rosario basalt (Central section; Fig. 4d–f), and the Santa Lucía basalt (Western section; Fig. 4g–i).

4.1. Petrography

4.1.1. Cúcamo basalt (eastern section)

These samples were collected from lava outcrops associated with the VESVF, specifically from the locality of Cúcamo (Fig. 2; Table 1). The main mineral assemblage is dominated by euhedral to subhedral tabular plagioclase crystals (57–60 %), also comprises euhedral to subhedral olivine (17–20 %) and phenocrystals of clinopyroxene, mainly augite (3–5 %) (Fig. 5a–c). The alteration of olivine into iddingsite is also observed (Fig. 5a). Accessory minerals include Ti-Fe-Mg oxides, accounting for approximately 7–11 % of the total mineral assemblage. This mineralogy displays general porphyritic and intergrowth-nodules textures (Fig. 5b), within a microcrystalline matrix conformed by a vitreous phase, microcrystalline plagioclase and iron oxides (hypocrystalline texture), with minor occurrence of vesicles (Fig. 5c).

4.1.2. El Rosario basalt (central section)

The units in this area are composed of mafic lava flows intercalated with scoria up to 5 m thick, characterized by abundant vesicles from 0.2 mm to 7 cm (Figs. 2 and 3). The mineralogy of this volcanic succession exhibits a groundmass composed mainly of plagioclase, olivine, clinopyroxene, orthopyroxene, and opaque oxides, exhibiting hypocrystalline and porphyritic textures, significant oxidation and the presence of vesicles (Fig. 5d–f). The main mineral assemblage comprises: (i) euhedral to subhedral olivine phenocrysts (14–20 %), with sizes ranging from 0.1 to 0.7 μm, some of which are often altered to iddingsite phase (Fig. 5d–e); (ii) euhedral to subhedral microcrystalline plagioclase (53–62 %); (iii) clinopyroxenes, mainly augite as subhedral crystals (3–7 %) with grain size around to 0.2 μm. In addition, a reaction rim is observed in orthopyroxenes (Fig. 5e); (iv) opaque minerals are accounting for 2–4 % of the assemblage (Fig. 5f). In addition, a reaction corona is observed in orthopyroxenes (Fig. 5f), this is a possible result of changes in thermodynamic conditions.

4.1.3. Santa Lucía basalt (western section)

These basaltic samples were collected from mafic lava walls and cinder cones (Fig. 2). It is important to mention the presence of peridotite xenoliths (Fig. 4h) and feldspathic granulites in this area. The mineralogical framework of these mafic rocks is characterized by a microcrystalline groundmass exhibiting a well-defined porphyritic texture, composed mainly of fine-grained, single-twinned plagioclase (53–57 %), together with pyroxene (3–7 %) and olivine (7–13 %), which occasionally displays iddingsite alteration (Fig. 5g). Some phenocrystals of brown amphibole phenocrysts, compositionally compatible with kaersutite and/or pargasite, were identified, as also reported by reported by Dávalos-Elizondo et al. (2016). Opaque minerals-oxides (Fig. 5g)

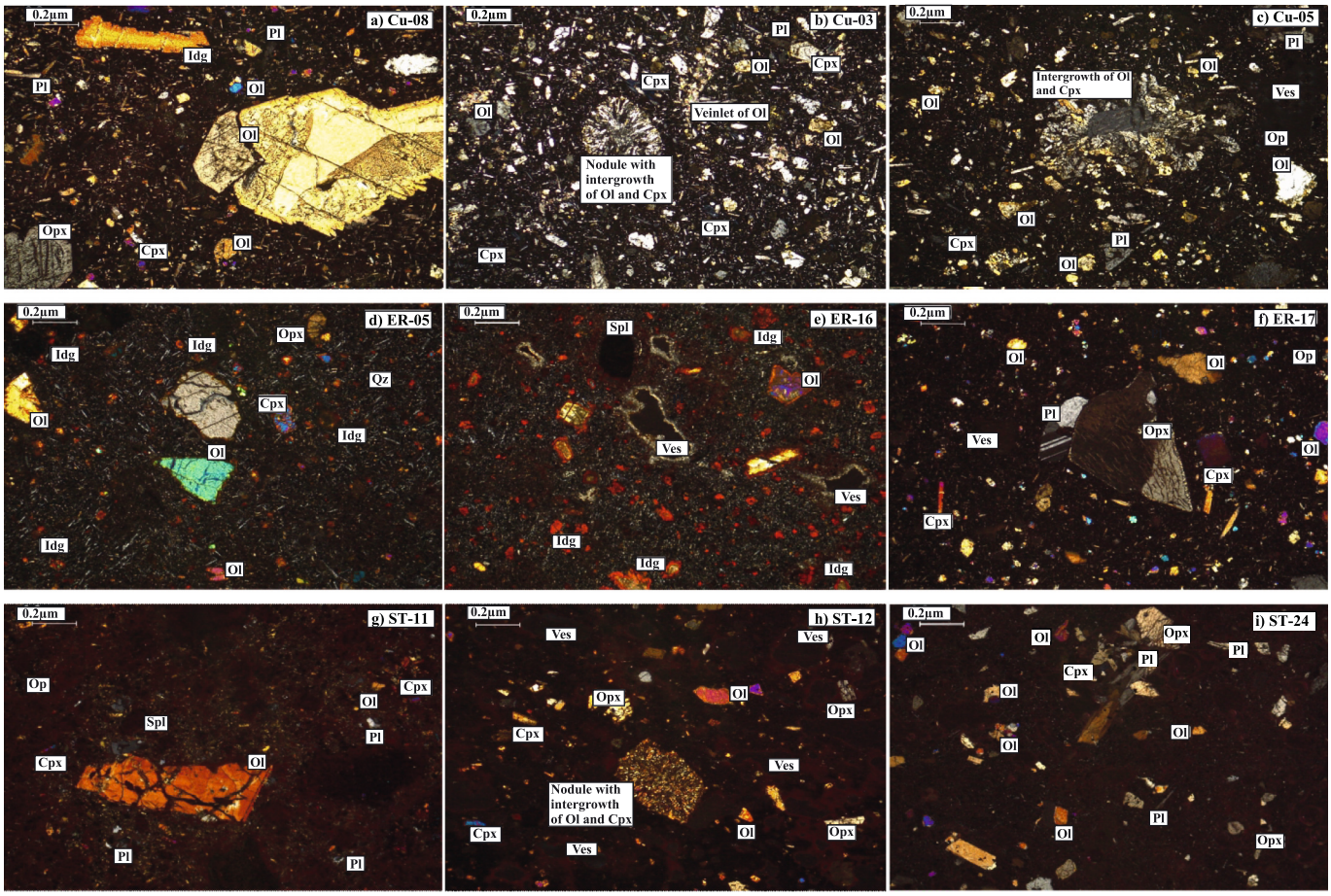

Fig. 5. Photomicrographs of basalts from the Cúcamo–Santa Lucía area, VESVF: (Fig. 5a–c) thin sections of mafic rocks from the Cúcamo basalt: (a) phenocrysts of Ol and pyroxene (Opx, Cpx) with Idg as an alteration product; (b) crystals of Ol and Cpx, and subordinate Pl with simple twinning, in a microcrystalline matrix, including an intergrowth nodule of Ol and pyroxene (Px); (c) crystals of Ol, Cpx, and Pl. (Fig. 5d–f) thin sections of mafic rocks from the El Rosario basalt: (d) trachybasalt with phenocrysts of Ol, Cpx, and Opx, abundant Idg in a microcrystalline matrix; (e) advanced alteration in a microcrystalline matrix; (f) trachybasalt with Ol, Cpx, phenocryst of Opx, and Pl in a hypocrystalline matrix. (Fig. 5g–i) thin sections of mafic rocks from the Santa Lucía basalt: (g) basalt with Ol, Cpx, and Idg in a glassy matrix; (h) basanite with altered Ol, phenocrysts of Cpx, and Idg alteration; (i) basanite with a veinlet composed of Cpx, Ol, Qz, and Pl in a microcrystalline matrix. Mineral abbreviations: Pl–plagioclase; Ol–olivine; Cpx–clinopyroxene; Opx–orthopyroxene; Idg–iddingsite; Op–opaque mineral; Ves–vesicle; Qz–quartz.

occur as secondary mineral phase (17–20 %). Vesicles and nodules of olivine, plagioclase, and clinopyroxene crystals with reaction rims are locally observed within the groundmass (Fig. 5h). A moderate degree of oxidation is also observed, pervasively intergrown within the groundmass and contributing to the development of the reaction rims around some phenocrystals (Fig. 5g–i).

4.2. *Whole rock geochemistry*

In addition to the 34 samples, reported in this work (Table 2), the additional literature data were also compiled from the following references: Luhr et al. (1989; n = 4 samples from SDVF, and n = 14 samples from VESVF), Luhr et al. (1995a, n = 15 samples from LEVF), Rivera-García et al. (2023, *n* = 13 samples) and Elizondo-Pacheco et al. (2022, n = 7 samples from Eastern Mexican Alkaline Province (EMAP)), Luhr et al. (1995b, n = 32 samples) and Valdez-Moreno et al. (2011, n = 13 samples from Mexican Quaternary Volcanic Complex (MQVC)) and Cousens et al. (2012, 2013, n = 4 and 13 samples from Basin and Range Province (BRP)) for comparison. In addition, these geochemical data were processed with the software IgRoCS (Verma and Rivera-Gomez, 2013) to adjust the iron oxidation along with other major oxides to sum of 100 % sum on an anhydrous basis and to calculate the CIPW norm. Based on adjusted silica content, the rocks display the following adjusted SiO_2 ranges: Cúcamo (SiO_2 < 48.63 wt%, *n* = 9), El Rosario (SiO_2 < 48.80 wt%, *n* = 11), and Santa Lucia (SiO_2 < 48.73 wt%, *n* = 14). The mafic rocks can be subdivided into: (i) *nepheline*-normative alkaline samples (8 from Cúcamo, 3 from El Rosario, and 5 from Santa Lucia) and (ii) *hypersthene*-normative subalkaline samples (1 from Cúcamo, 8 from El Rosario, and 9 from Santa Lucia). Classification using the total alkali–silica (TAS) diagram (Le Bas et al., 1986; Fig. 6a) places these rocks in the fields of basanite, basalt, and trachy-basalt (Fig. 6a). Moreover, they define a calc-alkaline to shoshonitic affinity (Fig. 6b).

4.2.1. *Cúcamo basalt (eastern section)*

The Cúcamo basaltic samples plot within the fields of basanites and trachybasalt (Fig. 6a). Their compositions are characterized by adjusted contents of $(SiO_2)_{adj}$ = 45.76–48.63 wt%, $(Al_2O_3)_{adj}$ = 13.81–16.58 wt %, $(MgO)_{adj}$ = 7.01–7.82 wt%, $(Na_2O)_{adj}$ = 8.57–10.88 wt%, $(K_2O)_{adj}$ = 2.23–3.73 wt%, $(TiO_2)_{adj}$ = 1.61–2.06 wt% (Table 2). The Mg# (calculated as 100 × $Mg^{2+}/(Mg^{2+} + Fe^{2+})$) = 52.27 to 63.51 (Table 2). CIPW normative calculation indicates nepheline contents of 3.00–7.98 wt%, and hypersthene of up to 7.99 wt% (Table 2). The subscript "adj" refers to the major-element data adjusted to 100 % on an anhydrous basis and after Fe-oxidation ratio adjustment; Verma and Rivera-Gomez, 2013). The mafic rocks exhibit negative correlations of SiO_2, TiO_2, FeO, CaO, and Ni with MgO, whereas they display a positive correlation

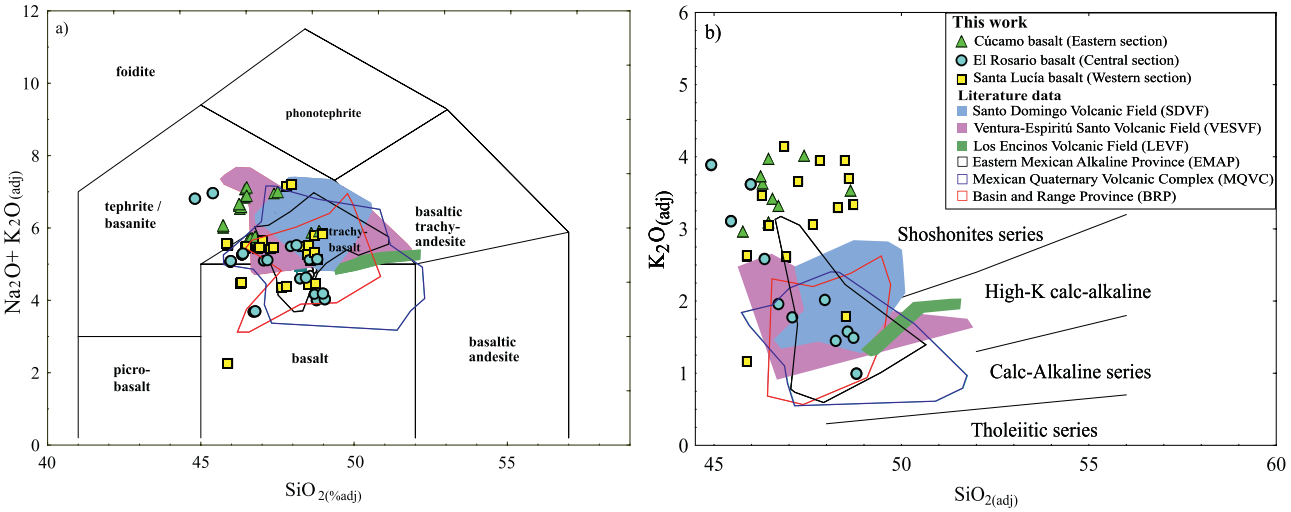

Fig. 6. a) Total alkali-silica classification diagram (TAS; Le Bas et al., 1986) and b) SiO_2 vs K_2O diagram by Peccerillo and Taylor (1976) for the mafic rocks, VESVF.

between Cr and MgO (Fig. S1, see supplementary material). Trace element compositions show Sc = 0.85–7.62 ppm, Cr = 19.30–141.29 ppm, Ni = 12.09–65.63 ppm and slightly enrichment in large ion lithophile element (LILE) Rb = 4.26–14.08 ppm, Ba = 50.23–101.02 ppm, Sr = 120.62–389.32 ppm, U = 0.45–0.64 ppm (Table 2).

The chondrite-normalized REE diagram (Fig. 7a) shows an enrichment in LREEs relative to heavy rare earth elements (HREEs), with $(La/Sm)_{CN}$ values ranging from 2.97 to 3.61 and $(La/Yb)_{CN}$ values between 18.91 and 29.51 and absence of an Eu anomaly (Table 2). Here, the subscript "CN" denotes values normalized to chondrite (McDonough and Sun, 1995). The primitive mantle–normalized multi-element diagram for the Cúcamo samples (Fig. 7d) displays a slightly enriched pattern in LILE and a generally decreasing trend towards the more compatible elements. The patterns are characterized by the absence of Nb anomalies (Nb/Nb* = 1.51–2.67), but they exhibit prominent positive anomalies in K, P, and Ti, together with a distinct negative anomaly in Pb*.

4.2.2. El Rosario basalt (central section)

The rocks from this area are classified as potassium trachybasalt, basalt and basanites (Fig. 6a). The volcanic rocks of El Rosario exhibit adjusted ($_{adj}$) compositions of $(SiO_2)_{adj}$ = 44.91–48.80 wt%, $(Al_2O_3)_{adj}$ = 13.98–19.05 wt%, $(MgO)_{adj}$ = 5.49–7.59 wt%, $(Na_2O)_{adj}$ = 7.93–10.67 wt%, $(K_2O)_{adj}$ = 1.43–3.78 wt%, $(TiO_2)_{adj}$ = 1.56–2.29 wt %, Mg# = 41.82–56.18, and a normative nepheline and hypersthene ranges of 0.877–8.30 wt% and 0.20–28.7 wt%, respectively (Table 2). The mafic rocks exhibit negative correlations of SiO_2, TiO_2, FeO, CaO, and Ni with MgO, whereas they display a positive correlation between Cr and MgO (Fig. S1). The El Rosario basalt display trace element concentrations of Sc = 0.76–22.54 ppm, Cr = 13.79–93.11 ppm, and Ni = 7.08–69.87 ppm, Table 2). The REE diagram (Fig. 7b) normalized to chondrite shows enrichment in LREEs compared to the HREEs ($(La/Sm)_{CN}$ = 2.22–3.48, $(La/Yb)_{CN}$ = 14.39–20.34) and absence of an Eu anomaly. The primitive mantle–normalized multi-element diagram (Fig. 7e) exhibits positive anomalies of K, P, and Ti with a negative anomaly in Pb*.

4.2.3. Santa Lucía basalt (western section)

The Santa Lucía rock samples are classified as trachybasalts and basalts (Fig. 6a). The mafic samples show compositions of $(SiO_2)_{adj}$ = 45.88–49.78 wt%, $(MgO)_{adj}$ = 4.68–7.18 wt%, $(Al_2O_3)_{adj}$ = 16.10–20.53 wt%, $(Na_2O)_{adj}$ = 9.00–11.38 wt%, $(K_2O)_{adj}$ = 1.01–3.18 wt%, Mg# = 37.84–54.78, and a normative nepheline and hypersthene ranges of 0.438–5.46 wt% and 3.82–24.7 wt% (Table 2). The mafic rocks exhibit negative correlations of SiO_2, TiO_2, FeO, CaO, and Ni with MgO, whereas they display a positive correlation between Cr and MgO (Fig. S1). Trace element compositions for the Santa Lucia basalt show Sc = 4.32–9.98 ppm, Cr = 32.45–128.82 ppm, and Ni = 31.56–158.22 ppm (Table 2).

Similar to other localities of the VESVF, the Santa Lucía basalts display enrichment in LREEs, with $(La/Sm)_{CN}$ = 2.97–3.23 and $(La/Yb)_{CN}$ = 14.04–15.13, alongside a relative depletion in HREEs (Fig. 7c) and absence of an Eu anomaly. The primitive mantle–normalized multi-element diagram (Fig. 7f) reveals positive anomalies in Ti and P, along with negative anomaly in Pb*.

4.3. Whole rock Sr-Nd isotopic data

Whole-rock Sr and Nd isotopic analyses were conducted on six mafic rock samples (Table 3; Fig. 8a–b). These results are compared with those from mafic rocks of the Eastern Mexican Alkaline Province (EMAP), Mexican Quaternary Volcanic Complex (MQVC), and Basin and Range Province (BRP) regions. Initial Sr isotope compositions versus εNd(t) values for the mafic rocks of Cúcamo, El Rosario, and Santa Lucía are presented in Fig. 8a–b, along with comparative data from other volcanic rocks of EMAP, MQVC, and BRP. The mafic rocks from the northwestern section of the VESVF display initial $^{87}Sr/^{86}Sr$ isotopic ratios (ISr) ranging from 0.703071 to 0.703525 and εNd(t) values between +5.7 and + 6.3 (Table 3). An estimated age of 1.1 Ma was taken for the calculation of the initial ratios of Sr-Nd isotopic data, with no significant radiogenic ingrowth affecting the present-day measured values. This age is based on the previously reported K-Ar determination for la Joya Honda (1.10 ± 0.21 Ma; Aranda-Gómez and Luhr, 1996).

5. Discussion

5.1. Petrographic features

The general mineralogical assemblage of the VESVF mafic rocks is dominated by tabular plagioclase, majorly as fine-grained size. Clinopyroxene (augite) and euhedral to subhedral olivine are also present together with secondary minerals such as Fe-Ti-Mg oxides and amphiboles. The occurrence of reaction rims in pyroxenes and olivine, the partially alteration of olivine into iddingsite phase and the significant degree of oxidation indicates that magma experienced changes in thermodynamic conditions or volatile content (hydrothermal processes) during its evolution. Texture framework (phenocrysts set in a fine-grained and hypocrystalline to intergranular matrix) suggests an initial slow crystallization of mafic phase at depth, followed by rapid

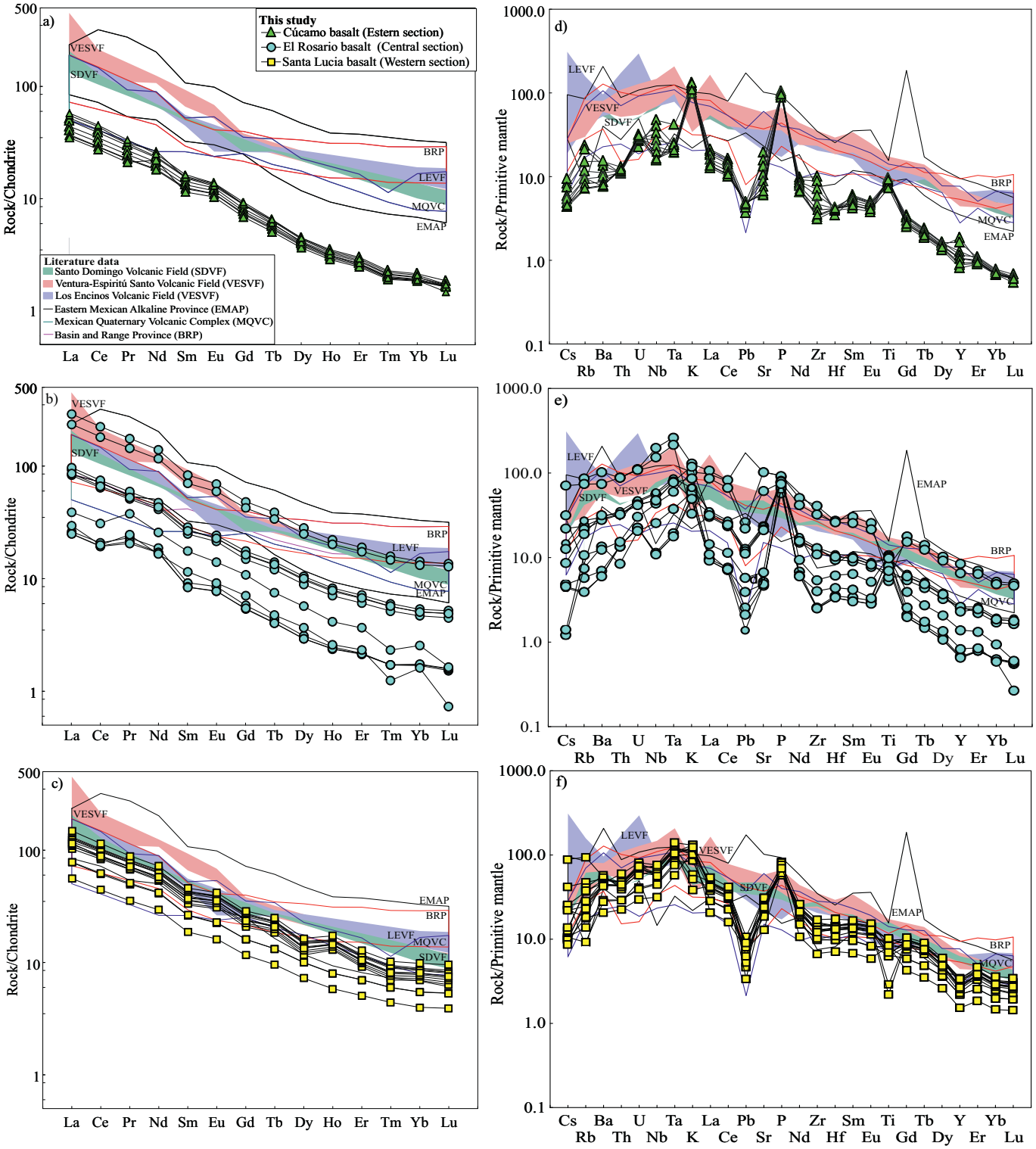

Fig. 7. a) Chondrite normalized rare-earth element (REE) diagrams for mafic rocks, VESVF; b) Primitive mantle normalized multielement diagrams for mafic rocks, VESVF (values for normalization were taken from McDonough and Sun, 1995).

magma ascent, indicated by the high content of plagioclase microcrystals in the groundmass (Lucci et al., 2020). The presence of vesicles further indicates degassing and fast solidification near the surface. This mineral arrangement and the textural characteristics support the mafic character of the VESVF rocks. Moreover, the forsterite composition of olivine together with the sporadic presence of brown amphibole (kaersutite and/or pargasite) is consistent with an upper mantle-derived magma (e.g., Dávalos-Elizondo et al., 2016; Lucci et al., 2024).

5.2. *Magmatic source and petrogenetic processes*

The VESF mafic rocks show an evidence of an upper mantle partial melting followed by a limited fractional crystallization of olivine ± orthopyroxene + clinopyroxene + plagioclase ± kaersutite + opaque

Table 3
Whole rock Sr–Nd isotopic data of mafic rocks from the VESVF. For εNdt CHUR values for $^{143}Nd/^{144}Nd = 0.512638$ and $^{147}Sm/^{144}Nd = 0.1967$ were taken from Jacobsen and Wasserburg (1980). Decay constant for ^{147}Sm: $6.54 \times 10\text{–}12\ y^{-1}$ (Lugmair and Marti, 1978). Rb, Sr, Sm and Nd concentrations were taken from Table 2.

Sample	Rock unit	Magma type	Age	Rb (ppm)	Sr (ppm)	$^{87}Rb/^{86}Sr$	$^{87}Sr/^{86}Sr$	±2σ	$^{87}Sr/^{86}Sr$ (i)	Sm (ppm)	Nd (ppm)	$^{147}Sm/^{144}Nd$	$^{143}Nd/^{144}Nd$	±2σ	$^{143}Nd/^{144}Nd$ (i)	εNd_t
Cu-01	Cucamo	Basic	1.1	14.8	389.32	0.1046	0.70321	2	0.70320	2.26	12.15	0.1126	0.51295	2	0.51295	6.0
Cu-09	Cucamo	Basic	1.1	5.75	120.62	0.1379	0.70309	2	0.70308	1.70	10.04	0.1022	0.51293	2	0.51293	5.8
ER-14	El Rosario	Basic	1.1	51.40	2047.09	0.0726	0.70353	2	0.70353	12.33	63.59	0.1172	0.51295	2	0.51295	6.2
ER-17	El Rosario	Basic	1.1	16.50	467.92	0.1020	0.70307	2	0.70307	4.27	21.69	0.1191	0. 51295	2	0.51295	6.1
SL-14	Santa Lucía	Basic	1.1	10.98	615.22	0.0516	0.70308	2	0.70307	6.36	30.27	0.1272	0. 51296	2	0.51296	6.3
SL-25	Santa Lucía	Basic	1.1	15.43	490.33	0.0910	0.70309	2	0.70308	5.31	25.27	0.1272	0. 51295	2	0.51295	6.0

minerals (Lucci et al., 2024 and references therein), as indicated by petrographic textures, mineral assemblages, and relatively low Mg# values (37.8–56.1). Variations in plagioclase, pyroxene, and olivine chemical compositions further support this interpretation. Elemental covariations in Harker diagrams (Fig. S1), suggests a low degree of fractionation of multiple phases: Ni, Cr, and MgO trends indicate olivine and clinopyroxene removal; negative TiO_2–MgO and FeO^T–MgO correlations indicate Fe-Ti oxide fractionation; and slightly negative SiO_2–MgO and CaO–MgO trends suggest plagioclase involvement. Collectively, these geochemical patterns indicate magma genesis of the VESF occurred by partial melting whereas their evolution could be related to fractional crystallization or assimilation.

In addition, immobile trace element ratio diagrams were employed (Fig. 9a–b) to understand this processes. Bivariate plots of Nb/Yb vs Th/Yb and Ta/Yb vs Th/Yb (Fig. 9a–b) indicate that the mafic volcanic rocks trend towards the mantle array, with compositions resembling those of OIB. In addition, the rocks exhibit LREE enrichment with fractionated profiles inclined towards the HREE, suggesting derivation from an enriched mantle source (Hirschmann et al., 1998; Fig. 7a–c). Furthermore, isotopic data plot within the mantle array, with Nd isotopic compositions relatively enriched compared to the bulk earth, whereas Sr isotopic compositions are more depleted. Together, these features are consistent with a slightly enriched mantle source (Fig. 8a–b).

According to Cullers and Graf (1984), REE patterns are useful indicators of melting conditions, where low degree of partial melting typically produces steeply fractionated REE trends, whereas higher degrees of melting generally yield flatter REE patterns (Cullers and Graf, 1984; Hirschmann et al., 1998). In the case of the mafic volcanic rocks of the VESVF, the steep HREE trend (Fig. 7a–c) and bivariate diagrams of Zr/Y vs Nb/Y and Zr/Nb vs Ce/Y (Fig. 10a–b) show low degrees of partial melting form an enriched mantle source. To further evaluate the relative effects of partial melting and/or fractional crystallization processes, the VESVF mafic samples were plotted in bivariate diagrams of immobile trace elements ratios (Fig. 11a–b). These diagrams indicate variable degrees of partial melting as the dominant process, rather than significant fractional crystallization, in controlling the geochemical signatures of the mafic volcanic rocks.

Therefore, to provide a better understanding related to the magmatic processes that affect the mafic rocks of the VESVF, we have developed a quantitative approach based on batch partial melting equations reported by Zou (2007). Initial magmas derived from garnet-lherzolite (Frey, 1980) and spinel-lherzolite (McDonough, 1990) were considered to the development of batch partial melting (Table S1, see supplementary material). The modal compositions for the bivariate melting models (Fig. 12a–c) were selected following those proposed by Pearson et al. (2014) and Aguirre Espinosa et al. (2022), and are as follows: (i) for the spinel-lherzolite source: 0.66 olivine (ol) + 0.24 orthopyroxene (opx) + 0.08 clinopyroxene (cpx) + 0.02 spinel (sp); and (ii) for the garnet-lherzolite source: 0.63 olivine (ol) + 0.30 orthopyroxene (opx) + 0.02 clinopyroxene (cpx) + 0.05 garnet (gt). The bivariate melting models account for relatively low-degrees partial melting between 0.1 % and 3 % (Fig. 12a–c).

The bivariate trace elements partial melting models (Fig. 12a–c) indicate that the mafic volcanic rocks of the VESVF are related to the result of partial melting from upper lithospheric mantle sources, consisting of enriched lherzolite. These sources are inferred to have undergone low degrees of partial melting, ranging from 1 % to 2 % (Fig. 12a–c). Additionally, average trace element ratio values for the San Luis Potosí xenoliths (Fig. 12a–c) have been included for comparison with the mafic volcanic rocks. Notably, the San Luis Potosí xenoliths exhibit lower concentrations than the mafic volcanic rocks of the VESVF, indicating an indirect relationship and suggesting a mantle source that is more enriched in LREEs. Furthermore, previous studies addressing magmatic processes and mantle sources in mafic volcanic rocks from the northern sector of the San Luis Potosi Volcanic Field support similar interpretations. For instance, Luhr et al. (1989) proposed that the Santo

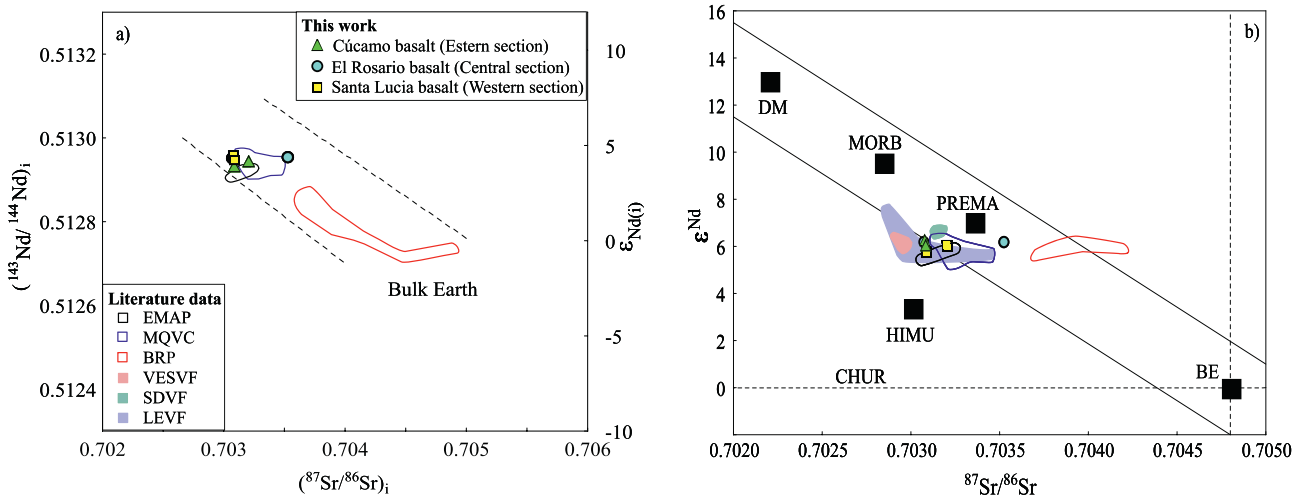

Fig. 8. Diagrams of isotopic ratios of mafic rocks, VESVF: a) $^{87}Sr/^{86}Sr_{(i)}$ vs $^{143}Nd/^{144}Nd_{(i)}$; b) $^{87}Sr/^{86}Sr_{(i)}$ vs ε_{Nd}. Abbreviation: DM–Depleted Mantle, MORB–Mid-Ocean Ridge Basalt, PREMA– Prevalent Mantle.

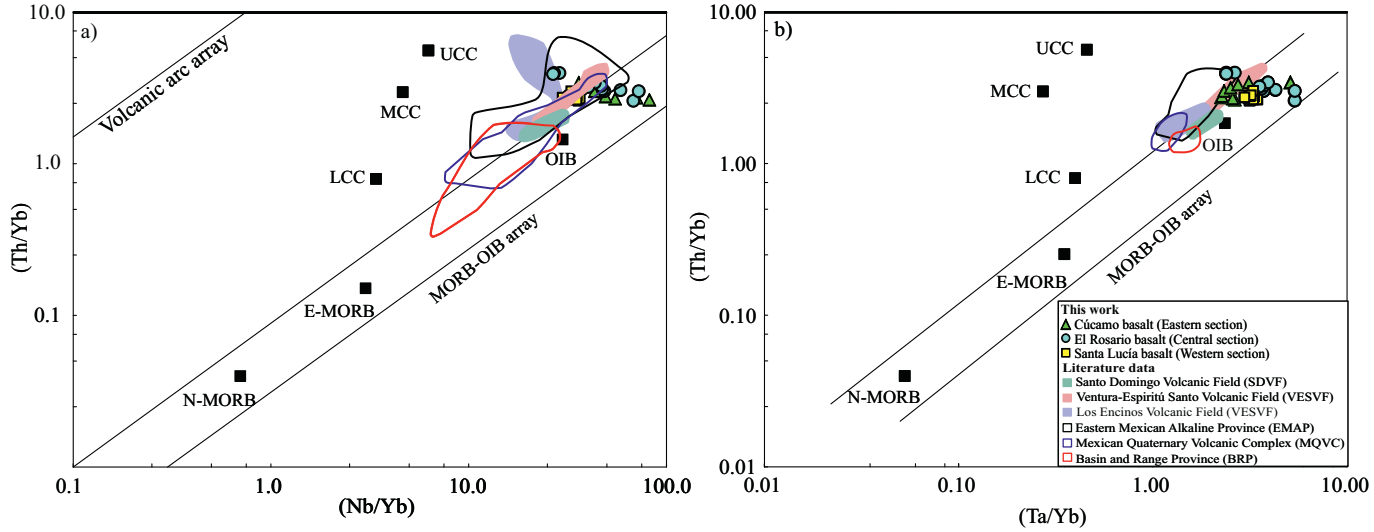

Fig. 9. Trace elements based bivariate diagrams of (a) Nb/Yb vs Th/Yb, (b) Ta/Yb vs Th/Yb for the magma source. Abbreviations: N-MORB–normal Mid-Ocean Ridge basalt, E-NORM–enriched Mid-Ocean Ridge basalt, OIB–Ocean Island basalt, LCC–Lower Continental Crust, MCC–Mid Continental Crust, UCC–Upper Continental Crust.

Domingo volcanic rocks were generated through progressive degrees of partial melting from a garnet peridotite mantle source. Similarly, Verma et al. (2023) presented geochemical models for mafic volcanic rocks from the Ahualulco area, suggesting their origin from low degrees of partial melting of a spinel-lherzolite mantle source. The results of the present study indicate that low-degree melting of an enriched lherzolite source also contribute to the VESVF mafic volcanic rocks, providing additional support for the hypothesis proposed by previous studies from the surrounding areas (Luhr et al., 1989; Verma et al., 2023 and references therein). Furthermore, petrographic and textural evidence, particularly the sporadic presence of amphibole phenocrysts (kaersuite and/or pargasite) and the fine-grained to intergranular matrix observed in the studied samples, suggests that magmas were derived from upper lithospheric mantle sources, where the generated melts suffer an initial slow crystallization followed by rapid ascent (Lucci et al., 2020; Lucci et al., 2024 and references therein). Such a scenario involving the upper lithospheric mantle and rapid magma ascent could produce restitic amphibole, representing fragments of a disrupted mantle assemblage (Richter and Carmichael, 1993; Lucci et al., 2024). This may correspond to a peritectic assemblage of melt + clinopyroxene + orthopyroxene + plagioclase (Bailie et al., 2020; Lucci et al., 2024 and references therein), as well as microcrystals in the groundmass, both of which are notable features of the mafic volcanic rocks from the VESVF. Nevertheless, further geochemical, isotopic and experimental investigations are required to better constrain the nature and extent of the mantle source beneath the San Luis Potosí Volcanic Field.

5.3. *Tectonic settings*

5.3.1. *Nb and Ta anomalies*

The Nb and Ta anomalies behave as high-field-strength elements (HFSE) and are associated with their presence in the mantle, as well as their stability under various geological conditions such as pressure (P), temperature (T), and water content (H_2O). The behavior of Nb and Ta, both high field strength elements (HFSEs), with respect to their neighboring elements Ba, a large ion lithophile element (LILE), and La, a light rare earth element (LREE), can be summarized as follows:

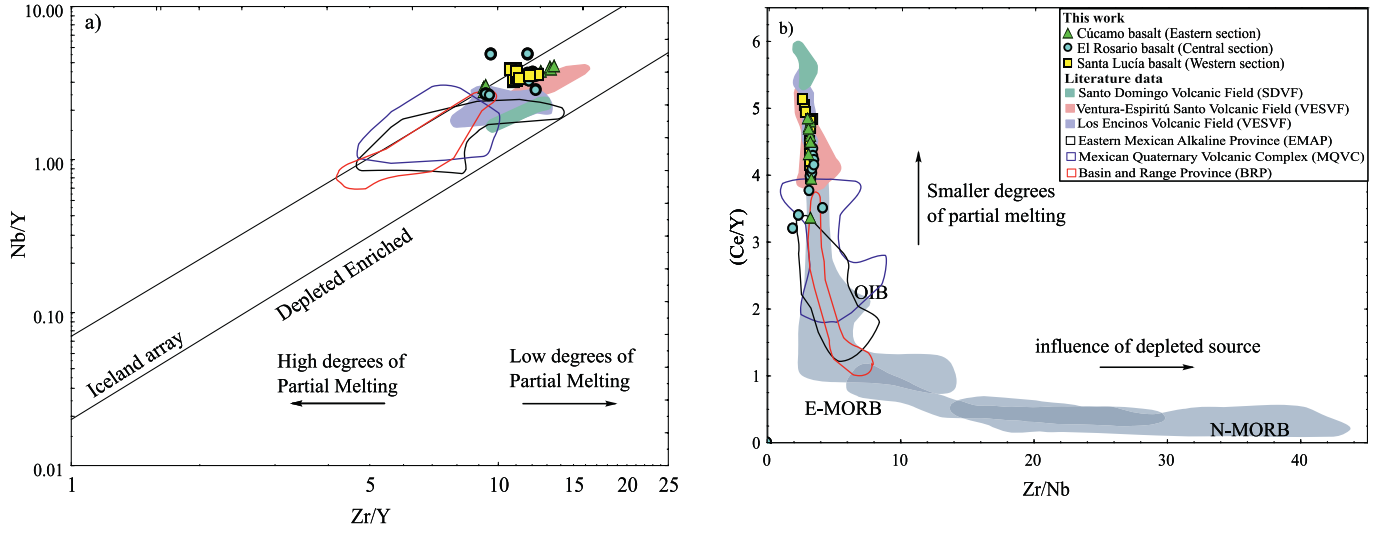

Fig. 10. (a) Zr/Y vs Nb/Y and (b) Zr/Nb vs Ce/Y show smaller degrees of partial melting source for the mafic rocks, VESVF.

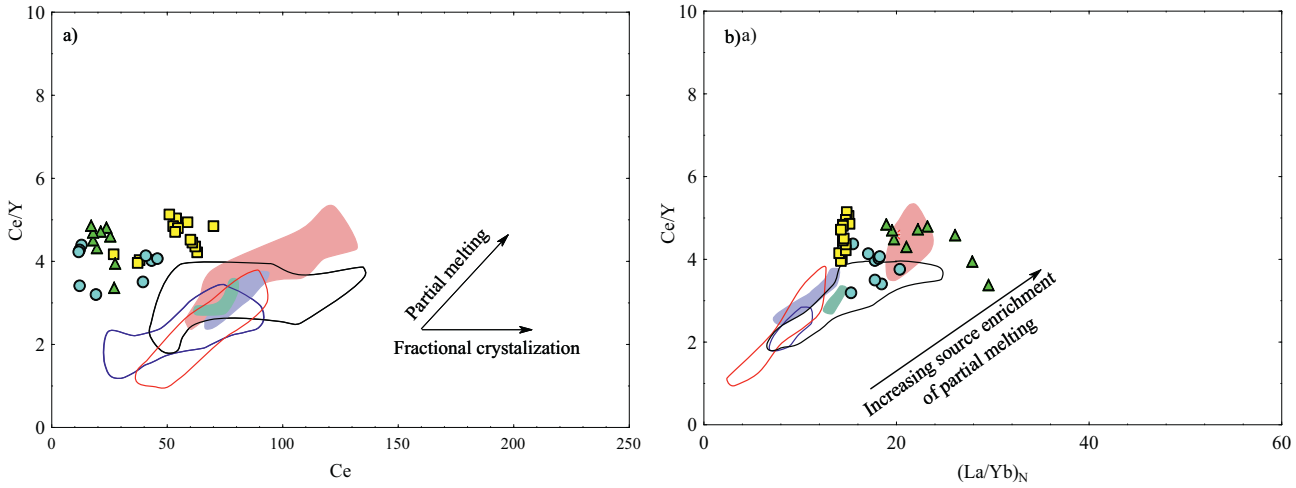

Fig. 11. (a) Ce vs Ce/Y; (b) $(La/Yb)_N$ vs Ce/Y diagrams indicate partial melt and fractional crystallization trend of the mafic rocks from the VESVF.

$$[Nb/Nb^*]_{PM} = \frac{2(Nb_{sample}/Nb_{PM})}{(Ba_{sample}/(Ba_{PM}) + (La_{sample}/(La_{PM})} \quad (1)$$

$$[Ta/Ta^*]_{PM} = \frac{2(Ta_{sample}/Ta_{PM})}{(Ba_{sample}/(Ba_{PM}) + (La_{sample}/(La_{PM})} \quad (2)$$

where the element symbols Nb, Ta, Ba, and La refer to the concentrations of these elements either in the sample or in the normalizing material; $[Nb/Nb^*]_{PM}$ and $[Ta/Ta^*]_{PM}$ represent the Nb and Ta anomalies, respectively, normalized to primitive mantle values.

In addition, intraplate magmas are typically characterized by elevated concentrations of Nb and Ta compared to magmas generated in arc settings, where these elements are often depleted due to subduction-related processes. Consequently, Nb and Ta concentrations, along with their anomalies, can serve as valuable geochemical indicators for distinguishing between different geodynamic settings. In this study, the mafic rocks exhibit Nb and Ta anomaly values ranging from 1.42 to 1.87, respectively (Table 4), which is close to continental rift and extension areas. The data for continental rift and extension areas were compiled from Verma (2015) and Verma et al. (2021). The values for mafic rocks have been considered in the case of the Cúcamo basalt (1.42 ± 0.12 and 2.47 ± 0.23), El Rosario basalt (1.82 ± 0.5 and 2.74 ± 0.61), and Santa Lucia basalt (1.87 ± 0.39 and 1.79 ± 0.45), being interpreted with affinities for a continental rift.

5.3.2. *Geochemical multi–dimensional discrimination diagrams*

About the tectonic implications, geochemical multi-dimensional discrimination diagrams were used. These diagrams are based on all major elements (Verma et al., 2006) and selected immobile trace elements (Agrawal et al., 2008) and processed through statistical techniques i.e., log-ratio transformation and liner discriminant analysis (LDA). These techniques make them more robust and efficient compared to other conventional bivariate and ternary diagrams (Verma et al., 2012, 2013). Furthermore, mafic rock samples were plotted in these diagrams (Fig. 13a–d), all samples (except one) are plotted in the field of continental rift basalt (CRB) in the diagrams of (Verma et al., 2006; Fig. 13a–b). In addition, all samples are also discriminated as continental rift basalt and ocean island basalt (CRB + OIB) in the diagrams of (Agrawal et al., 2008; Fig. 13c–d). Although, based on this observation, the tectonic environment for the VESVF mafic rocks was an extensional type intraplate magmatism during the Plio-Quaternary. Nevertheless, this tectonic setting inferred from the new multi-dimensional discrimination diagrams seem to be consistent with the geological evidence. Luhr and Aranda-Gómez (1997) described the origin and evolution of VESVF mafic rocks in a continental extension and are related to the

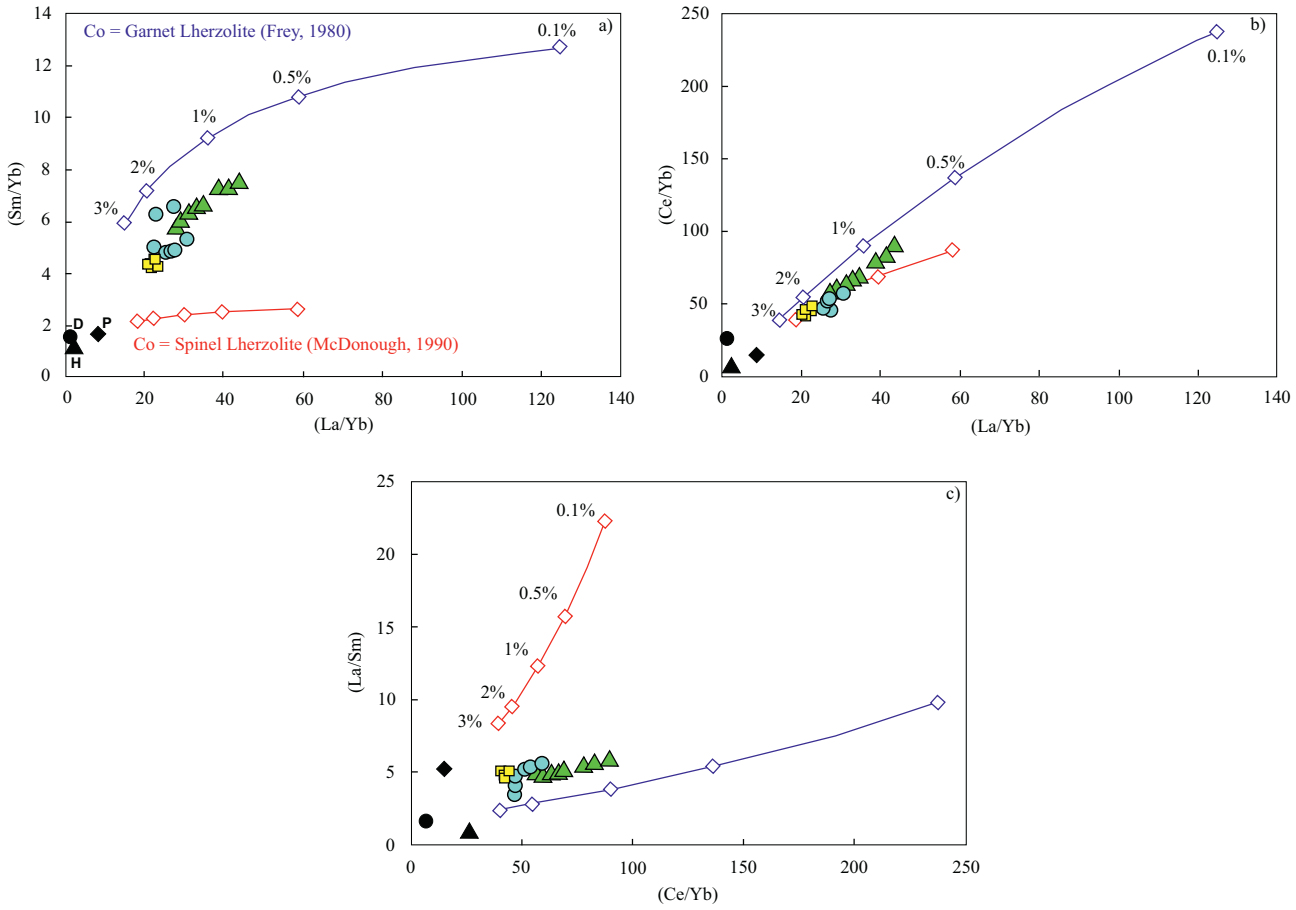

Fig. 12. Batch partial melting models for mafic rocks, VESVF: (a–d) the bivariate trace elements and REE partial melting with modal assemblage of 0.66 olivine (ol) + 0.24 orthopyroxene (opx) + 0.08 clinopyroxene (cpx) + 0.02 spinel (sp) for spinel-lherzolite and 0.63 olivine (ol) + 0.30 orthopyroxene (opx) + 0.02 clinopyroxene (cpx) + 0.05 garnet (gt) for the garnet-lherzolite source. The partial melting curves were generated following the batch melting equation of Zou (2007) using as initial magmas (C0): (i) spinel-lherzolite (taken from McDonough, 1990) in red line and (ii) garnet-lherzolite (taken from Frey, 1980) in blue line. Black lines represent-mixing curves between the two types of sources. Abbreviations: P = average lherzolite xenolith value reported by Pier et al. (1992): H = average lherzolite xenolith value reported by Heinrich and Besch (1992); D = average lherzolite xenolith value reported by Dávalos-Elizondo et al. (2016). (For interpretation of the references to color in this figure legend, the reader is referred to the web version of this article.)

Table 4
Nb and Ta anomaly statistic values (with respect to Ba and La) for mafic rocks from the VESVF, San Luis Potosi, Mexico (this work) and comparison with other continental arcs and rifts (taken from Verma, 2015; Verma et al., 2021).

Area	Magma type	$\{Nb/Nb\}^*_{pm}$		$\{Ta/Ta\}^*_{pm}$	
		Mean ± standard deviation (number of samples) x ± s (n)	99 % Confidence limits (CL) of the mean	Mean ± standard deviation (number of samples) x ± s (n)	99 % Confidence limits (CL) of the mean
Ventura Espíritu Santo Volcanic Field (VESVF)					
Cúcamo basalt	Basic	1.42 ± 0.12 (14)	1.20–1.59	2.47 ± 0.23 (14)	2.06–2.81
El Rosario basalt	Basic	1.82 ± 0.51(11)	1.38–3.22	2.74 ± 0.61 (11)	2.32–4.45
Santa Lucía basalt	Basic	1.87 ± 0.39 (9)	1.52–2.67	1.79 ± 0.45 (9)	1.13–2.46
Continental arcs					
Central American Volcanic Arc	Basic	0.13 ± 0.06 (59)	0.11–0.15	0.18 ± 0.11 (34)	0.13–0.23
Andes (Chile)	Basic	0.20 ± 0.05 (29)	0.17–0.23	0.147 ± 00.037 (9)	0.17–0.23
Continental rifts or extensional areas					
Rio Grande rift, New Mexico (USA)	Basic	0.7 ± 0.5 (29)	0.5–1.0	0.8 ± 0.5	0.5–1.1
Central Mexican Volcanic Belt	Basic	0.54 ± 0.25 (38)	0.43–0.65	0.75 ± 0.16 (30)	0.67–0.84
Eastern Anatolia (Turkey)	Basic	0.782 ± 0.014 (20)	0.773–0.791	0.784 ± 0.038 (20)	0.760–0.809
North and Northeast China	Basic	0.78 ± 0.17 (21)	0.67–0.88	0.49 ± 0.11 (4)	0.17–0.80

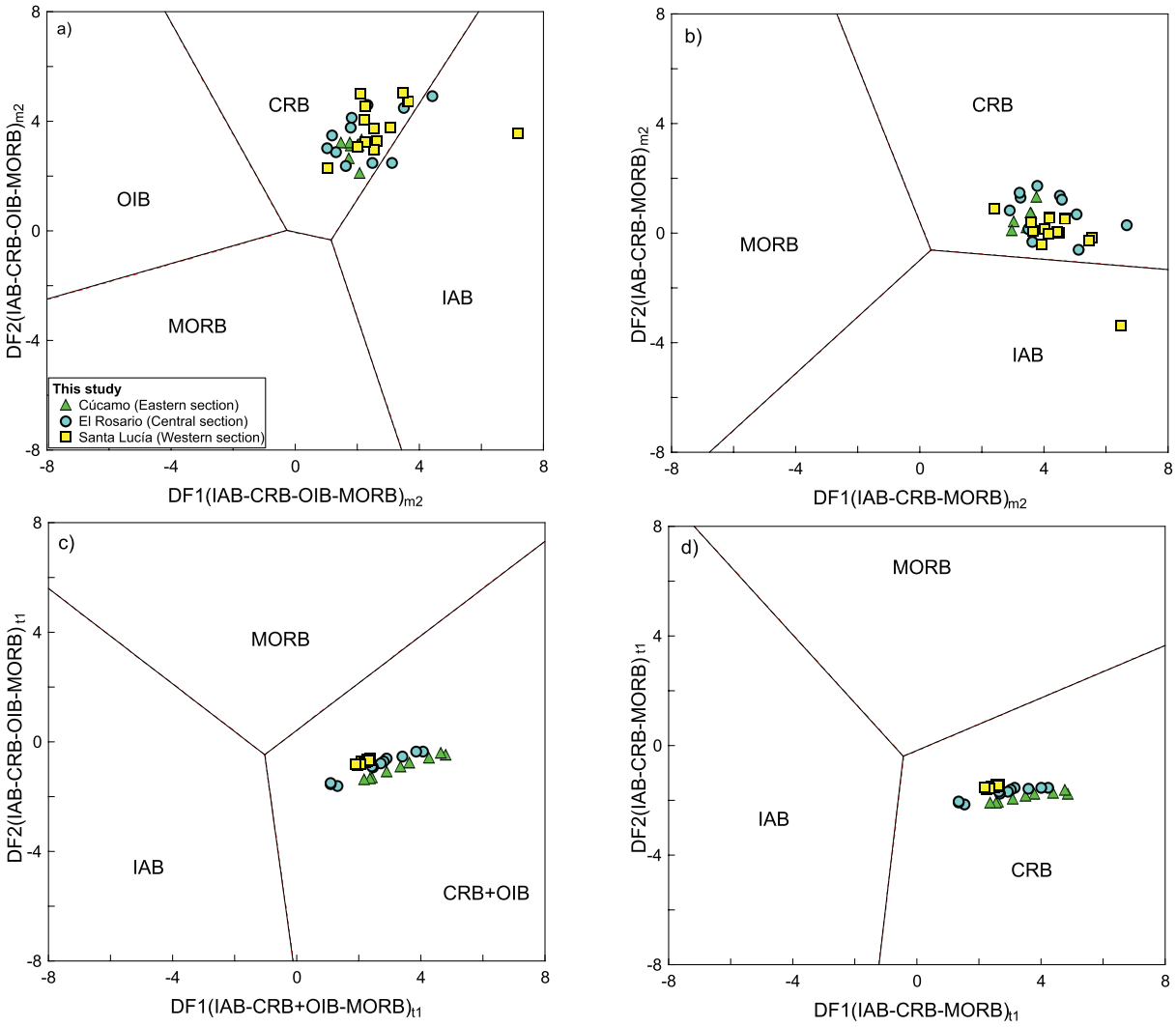

Fig. 13. (a–b) Multidimensional discrimination diagrams based on log-transformed proportions of major elements (Verma et al., 2006); (c–d) immobile trace elements (Agrawal et al., 2008) for the mafic rocks, VESVF. Abbreviations: MORB–Mid-Ocean Ridge Basalt; IAB–Island Arc Basalt; CRB–Continental Rift Basalt, OIB–Ocean Island Basalt.

stretching and depressurization from the lithosphere towards a more asthenospheric zone. These findings along with the geochemical (discrimination diagram) evidence reported in this work support an extensional environment for the VESVF.

5.4. Final considerations

Luhr et al. (1989) suggested that mantle upwelling beneath the VESVF crust was minimal, and that partial melting was likely the dominant process responsible for generating mafic volcanic rocks in the area. Furthermore, Sr-Nd isotopic data reported by Pier et al. (1989) indicate affinities with OIB sources for the magmatic rocks. Based on the geochemical and isotopic data obtained in the present study for the western VESVF, it is suggested that the mafic volcanic rocks are linked to both OIB-type and enriched mantle sources. Additionally, REE and trace element concentration patterns support the interpretation of an enriched mantle component contributing to the genesis of mafic volcanic rocks in the western VESVF. Geochemical modeling developed in this study indicates that these rocks were likely formed by low degrees (1–2 %) of partial melting from a spinel-lherzolite mantle source. We recognize that geochemical models are subject to uncertainties arising from the selected distribution coefficients, mineral assemblages, and mathematical assumptions (e.g., Torres-Sánchez et al., 2022). Nevertheless, this initial approach to understanding the magmatic processes controlling the formation of mafic rocks from the VESVF provides an important opportunity to further advance research in this and surrounding areas. Furthermore, these results strengthen the interpretation that the mafic magmatism in the VESVF and adjacent regions was predominantly generated by small degrees of partial melting of the mantle source. Similar to the northern portion of the SLPVF (Luhr et al., 1989), the VESVF appears to be characterized by enriched mantle source domains. Further research is recommended to better define the distinct mantle portions and magmatic systems throughout the SLPVF.

6. Conclusions

The VESVF mafic rocks exhibit tabular plagioclase, which commonly displays oscillatory zoning, reflecting chemical variations during crystallization. Euhedral to subhedral olivine and clinopyroxene (augite), are also present together with secondary minerals such as titanomagnetite and ilmenite, and the peridotite content, supporting the mafic character of the VESVF rocks. These features indicate an alkaline-subalkaline, mantle-derived magma, typical of a monogenetic volcanic field. Geochemical and isotopic data ($^{87}Sr/^{86}Sr_i = 0.703071–0.703525$; $^{143}Nd/^{144}Nd_i = 0.512932–0.512958$) indicate that mafic rocks were generated by low-degree (1–2 %) partial melting of an enriched

lherzolite upper lithospheric mantle source. Chondrite and primitive mantle-normalized REE and multi-element patterns, together with Nb-Ta behavior and multidimensional geochemical discrimination, suggest an extensional tectonic setting. These results support the interpretation that VESVF magmatism was closely linked to lithospheric extension highlighted the role of small-degree partial melting of the enriched lherzolite upper lithospheric mantle source.

Supplementary data to this article can be found online at https://doi.org/10.1016/j.chemer.2025.126355.

CRediT authorship contribution statement

Karla R. Hernández Martínez: Writing – original draft, Methodology, Investigation, Formal analysis. **Sanjeet K. Verma:** Writing – review & editing, Writing – original draft, Supervision, Project administration, Methodology, Investigation, Funding acquisition, Data curation, Conceptualization. **Darío Torres-Sánchez:** Writing – review & editing, Methodology, Investigation, Data curation. **Erik Emmanuel M. Torres:** Writing – review & editing, Methodology. **José R. Torres Hernández:** Writing – review & editing, Validation, Resources, Investigation. **Sonia A. Torres-Sánchez:** Writing – review & editing, Resources. **Hector Hernández-Mendoza:** Writing – review & editing, Formal analysis. **Juan Antonio Moreno:** Writing – review & editing, Visualization, Supervision, Resources. **José Manuel Fuenlabrada:** Writing – review & editing, Visualization, Validation, Software, Formal analysis, Data curation. **Beatriz A. Rivera-Escoto:** Validation, Formal analysis.

Declaration of competing interest

The authors declare that they have no known competing financial interests or personal relationships that could have appeared to influence the work reported in this paper.

Acknowledgments

KRHM thanks the Secretariat of Science, Humanities, Technology and Innovation (SECIHTI), Mexico for her doctorate scholarship (grant no. 932326). This doctoral thesis is carried on under supervision of SKV. SKV is grateful to Newton Advanced Fellowship award–The Royal Society, UK for the grant [NA160116]. We thank Ms. Maria Mercedes Zavala Arriaga for her support in the Laboratory of Applied Geology, Petrography and Petrophysics (Lab-GeoAPP), Division of Applied Geosciences, IPICYT. Our sincere thanks to Ms. Virginia Sánchez López for her support in isotopic analysis at the Geochronology unit, Complutense University of Madrid, Spain. We are grateful to the Editor-in-Chief (Prof. Astrid Holzheid) and the Associate Editor (Prof. Federico Lucci) for their efficient editorial handling and to the four anonymous reviewers for their constructive comments that helped improve the revised version of the manuscript.

References

Agrawal, S., Guevara, M., Verma, S.P., 2008. Tectonic discrimination of basic and ultrabasic rocks through log-transformed ratios of immobile trace elements. International Geology Review 50, 1057–1079.

Aguirre Espinosa, J.G., Velasco-Tapia, F., Rodríguez-Saavedra, P., Salinas-Jasso, J.A., 2022. Geochemometrics: petrology of quaternary volcanism in the Central Mexican Volcanic Belt. In: Armstrong-Altrin, J.S., Pandarinath, K., Verma, S.K. (Eds.), Geochemical Treasures and Petrogenetic Processes. Springer, Singapore. https://doi.org/10.1007/978-981-19-4782-7_14.

Aranda-Gómez, J.J., Luhr, J.F., 1996. Origin of the Joya Honda maar, San Luis Potosí, México. J. Volcanol. Geotherm. Res. 74, 1–18.

Aranda-Gómez, J.J., Luhr, J.F., Housh, Todd B., Valdez-Moreno, G., Chávez-Cabello, G., 2005. El volcanismo tipo intraplaca del Cenozoico tardío en el centro y norte de México: una revisión. Boletín de la Sociedad Geológica Mexicana 3, 187–225.

Bailie, R., Adriaans, L., le Roux, P., 2020. Peritectic assemblage entrainment as the main compositional driver in the I-type Vredenburg Granite, north-western Pan-African Saldania Belt, South Africa: a whole-rock chemical perspective. Lithos 364, 105522.

Centeno-García, E., 2005. Review of Upper Paleozoic and Lower Mesozoic stratigraphy and depositional environments of central and west Mexico: constraints on terrane analysis and paleogeography. In: Anderson, T.H., Nourse, J.A., McKee, J.W., Steiner, M.B. (Eds.), The Mojave-Sonora Megashear Hypothesis: Development, Assessment, and Alternatives, Geological Society of America Special Paper, 393, pp. 233–258.

Centeno-García, E., 2017. Mesozoic tectono-magmatic evolution of Mexico: an overview. Ore Geol. Rev. 81, 1035–1052.

Centeno-García, E., Guerrero-Suastegui, M., Talavera-Mendoza, O., 2008. The Guerrero Composite Terrane of western Mexico: collision and subsequent rifting in a supra-subduction zone. In: Draut, A., Clift, P.D., Scholl, D.W. (Eds.), Formation and Applications of the Sedimentary Record in Arc Collision Zones, Geological Society of America Special Paper, 436, pp. 279–308.

Centeno-García, E., Busby, C., Busby, M., Gehrels, G., 2011. Evolution of the Guerrero composite terrane along the Mexican margin, from extensional fringing arc to contractional continental arc. GSA Bull. 123, 1776–1797.

Cousens, B.L., Henry, C.D., Gupta, V., 2012. Distinct mantle sources for Pliocene–Quaternary volcanism beneath the modern Sierra Nevada and adjacent Great Basin, northern California and western Nevada, USA. Geosphere 8, 562–580.

Cousens, B., Wetmore, S., Henry, C.D., 2013. The Pliocene–Quaternary Buffalo Valley volcanic field, Nevada: post-extension, intraplate magmatism in the north-central Great Basin, USA. J. Volcanol. Geotherm. Res. 268, 17–35.

Cullers, R.L., Graf, J.L., 1984. Rare earth elements in igneous rocks of the continental crust: predominantly basic and ultrabasic rocks. Dev. Geochem. 2, 237–274.

Dávalos-Elizondo, M.G., Aranda-Gómez, J.J., Levresse, G., Cervantes de la Cruz, K.E., 2016. Química mineral y geoquímica de xenolitos del manto del campo volcánico Santo Domingo, San Luis Potosí: evidencias de procesos metasomáticos del manto bajo porciones de la Mesa Central, México. Revista Mexicana de Ciencias Geológicas 33, 81–104.

Del Pilar-Martínez, A., Nieto-Samaniego, A.F., Angeles Moreno, E., Suárez Arias, A.M., Olmos Moya, M.J.P., Alaniz Álvarez, S.A., Levresse, G., 2021. Digital geological map and geochronological database of the Cenozoic cover of the southern Mesa Central province, Mexico. Terra Digitalis 5, 1–10.

Dickinson, W.R., 2002. The Basin and Range province as a composite extensional domain. Int. Geol. Rev. 44, 1–38.

Dickinson, W.R., 2004. Evolution of the north American Cordillera. Annu. Rev. Earth Planet. Sci. 32, 13–45.

Elizondo-Pacheco, L.A., Ramírez-Fernández, J.A., De Ignacio, C., González-Guzmán, R., Rodríguez-Saavedra, P., Leal-Cuellar, V.A., Velasco-Tapia, F., Montalvo-Arrieta, J.C., 2022. Generation of arc-like and OIB-like magmas triggered by slab detachment in the Eastern Mexican Alkaline Province: petrological evidence from the Cenozoic Sierra de San Carlos-Cruillas Complex, Tamaulipas. J. Petrol. 63, 1–24.

Fitz-Díaz, E., Lawton, T.F., Juárez-Arriaga, E., Chávez-Cabello, G., 2018. The Cretaceous-Paleogene Mexican orogen: structure, basin development, magmatism and tectonics. Earth Science Review 183, 56–84.

Frey, F.A., 1980. The origin of pyroxenites and garnet pyroxenites from Salt Lake Crater, Oahu, Hawaii: trace element evidence. Am. J. Sci. 280A, 427–444.

Heinrich, W., Besch, T., 1992. Thermal history of the upper mantle beneath a young back-arc extensional zone: ultramafic xenoliths from San Luis Potosí, Central México. Contrib. Mineral. Petrol. 111, 126–142.

Hirschmann, M.M., Ghiorso, M.S., Wasylenki, L.E., Asimow, P.D., Stolper, E.M., 1998. Calculation of peridotite partial melting from thermodynamic models of minerals and melts. Method and composition to experiments. J. Petrol. 39, 1091–1115.

Jacobsen, S.B., Wasserburg, G.J., 1980. Sm–Nd isotopic evolution of chondrites. Earth and Planetary Science Letter 50, 139–155.

Labarthe–Hernández, G., Tristán–González, M., Aranda–Gómez, J.J., 1982. Revisión estratigráfica del Cenozoico de la parte central del Estado de San Luis Potosí: Universidad Autónoma de San Luis Potosí. Instituto de Geología y Metalurgia, Folleto Técnico, p. 85.

Le Bas, M., LeMaitre, R.W., Streckeisen, A., Zanettin, B., 1986. A chemical classification of volcanic rocks base on the total alkali-silica diagram. J. Petrol. 27, 745–750.

Lucci, F., Carrasco-Núñez, G., Rossetti, F., Theye, T., White, J.C., Urbani, S., Azizi, H., Asahara, Y., Giordano, G., 2020. Anatomy of the magmatic plumbing system of Los Humeros Caldera (Mexico): implications for geothermal systems. Solid Earth 11, 125–159.

Lucci, F., Cavazos-Alvarez, J.A., White, J.C., Sosa-Ceballos, G., Ruospo, D., Hermenegildo, N.S., Torres-Sánchez, D., Carrasco-Núñez, G., 2024. A window on the lithospheric mantle beneath the eastern Trans-Mexican volcanic belt: insights from pargasite-bearing mantle xenocrysts from the Holocene Ocotenco maar volcano. J. South Am. Earth Sci. 138, 104867.

Lugmair, G.W., Marti, K., 1978. Lunar initial 143Nd/144Nd differential evolution of the lunar crust and mantle. Earth Planet. Sci. Lett. 39, 349–357.

Luhr, J.F., Aranda-Gómez, J.J., 1997. Mexican peridotite xenoliths and tectonic terranes: correlations among vent location, texture, temperature, pressure, and oxygen fugacity. J. Petrol. 38, 1075–1112.

Luhr, J.F., Aranda-Gómez, J., Pier, J., 1989. Spinel-lherzolite-bearing Quaternary volcanic centers in San Luis Potosi, Mexico. 1. Geology, mineralogy, and petrology. J. Geophys. Res. 94, 7916–7940.

Luhr, J.F., Pier, J.G., Aranda-Gómez, J.J., Podosek, F., 1995a. Crustal contamination in early basin-and-range hawaiites of the Los Encinos Volcanic Field, central México. Contrib. Mineral. Petrol. 118, 321–339.

Luhr, J.F., Aranda-Gómez, J.J., Housh, T.B., 1995b. San Quintín Volcanic Field, Baja California Norte, México: geology, petrology and geochemistry. J. Geophys. Res. 100, 10353–10380.

Luhr, J.F., Kimberly, P., Siebert, L., Aranda-Gómez, J.J., Housh, T.B., Mattietti, G.K., 2006. México's quaternary volcanic rocks: insights from the MEXPET petrological and geochemical database. In: Siebe, C., Macías, J.L., Aguirre-Díaz, J. (Eds.),

Neogene-Quaternary Continental Margin Volcanism: A Perspective from México, 402. Geological Society of America, pp. 1–44.
McDonough, W.F., 1990. Constraints on the composition of the continental lithospheric mantle. Earth Planet. Sci. Lett. 101, 1–18.
McDonough, W.F., Sun, S.S., 1995. The composition of the Earth. Chem. Geol. 120, 223–253.
Nier, O.A., 1938. The isotopic constitution of strontium, barium, bismuth, thallium and mercury. Phys. Rev. 54, 275–278.
Nieto-Samaniego, A.F., Ferrari, L., Alaniz–Alvarez, S.A., Labarthe–Hernández, G., Rosas–Elguera, J., 1999. Variation of cenozoic extension and volcanism across the southern Sierra Madre Occidental volcanic province, Mexico. Geol. Soc. Am. Bull. 111, 347–363.
Nieto-Samaniego, A.F., Alanís-Álvarez, S.A., Camprubí, A., 2007. Mesa Central of México: stratigraphy, structure, and Cenozoic tectonic evolution. In: Alaniz-Álvarez, S.A., Nieto-Samaniego, Á.F. (Eds.), Geology of México: Celebrating the Centenary of the Geological Society of México, Geological Society of America Special Paper, 422, pp. 41–70.
Nieto-Samaniego, A.F., Del Pilar-Martínez, A., Suárez-Arias, A.M., Angeles-Moreno, E., Alaniz-Álvarez, S.A., Levresse, G., Xu, S., Olmos-Moya, M.J.P., Báez-López, J.A., 2023. Una revisión de la geología y evolución tectónica cenozoicas de la Mesa Central de México. Rev. Mex. Cienc. Geol. 40, 187–213.
O'Nions, R.K., Carter, S.R., Evensen, N.M., Hamilton, P.J., 1979. Geochemical and cosmochemical applications of Nd isotope analysis. Annu. Rev. Earth Planet. Sci. 7, 11–38.
Paz-Moreno, F.A., Demant, A., Cochemé, J.J., Dostal, J., Montigny, R., 2003. The Quaternary Moctezuma volcanic field: a tholeiitic to alkali basaltic episode in the central Sonoran Basin and Range Province, México. In: Johnson, S.E., Paterson, S.R., Fletcher, J.M., Girty, G.H., Kimbrough, D.L., Martín-Barajas, A. (Eds.), Tectonic Evolution of Northwestern Mexico and the Southwestern USA, 374. Geological Society of America, pp. 439–455.
Pearson, D.G., Canil, D., Shirey, S.B., 2014. Mantle samples included in volcanic rocks: xenoliths and diamonds. In: Treatise on Geochemistry (Second Edition), 3, pp. 169–253.
Peccerillo, A., Taylor, S.R., 1976. Geochemistry of Eocene calc–alkaline volcanic rocks from the Kastamonu Area, Northern Turkey. Contrib. Mineral. Petrol. 58, 63–81.
Pier, J.G., Podosek, F., Luhr, J.F., Brannon, J., Aranda-Gómez, J.J., 1989. Spinel-lherzolite-bearing, Quaternary volcanic centers in San Luis Potosí, México. II. Sr and Nd isotopic systematics. J. Geophys. Res. 94, 7941–7951.
Pier, J.G., Luhr, J.F., Podosek, F.A., Aranda-Gómez, J., 1992. The La Breña - El Jagüey Maar Complex, Durango, Mexico: II. Petrology and geochemistry. Bulletin of Volcanology 54, 405–428.
Richter, K., Carmichael, I.S., 1993. Mega-xenocrysts in alkali olivine basalts: fragments of disrupted mantle assemblages. Am. Mineral. 78, 1230–1245.
Rivera-García, J.J., Ramírez-Fernández, J.A., Velasco-Tapia, F., Salinas-Jasso, J.A., Orozco-Esquivel, M.T., Stockli, D., Leal-Cuellar, V.A., Elizondo-Pacheco, L.A., 2023. Constraints on the origin of the cenozoic intraplate aldama volcanic field, Tamaulipas, NE México. J. South Am. Earth Sci. 129, 104508.
Shukla, M., Verma, S.K., Ramos-Vázquez, M.A., Armstrong-Altrin, J.S., Hernández-Martínez, K.R., Mishra, S., Malviya, V.P., Hernández-Mendoza, H., 2024. Geochemistry and mineralogy of beach sediments in the northern Gulf of Mexico, Tamaulipas state, Mexico: implication for provenance. J. Palaeogeogr. 3, 375–400.
Tanaka, T., Togashi, S., Kamioka, H., Amakawa, H., Kagami, H., Hamamoto, T., Yuhara, M., Orihashi, Y., Yoneda, S., Shimizu, H., Kunimaru, T., Takahasi, K., Yonagi, T., Nakano, T., Fujimaki, H., Sjijo, R., Asahara, Y., Tanimizu, M., Dragusanu, C., 2000. JNdi-1: a neodymium isotopic reference in consistency with La Jolla neodymium. Chem. Geol. 168, 279–281.
Torres-Hernández, J.R., Labarthe-Hernández, G., Aguillón-Robles, A., Gómez-Anguiano, M., Mata-Segura, J.L., 2006. The pyroclastic dikes of the Tertiary San Luis Potosi volcanic field: implications on the emplacement of Panalillo ignimbrite. Geofis. Int. 45, 243–253.
Torres-Sánchez, D., Verma, S.K., Verma, S.P., Velasco-Tapia, F., Torres-Hernández, J.R., 2019. Petrogenetic and tectonic implications of Oligocene-Miocene volcanic rocks from the Sierra de San Miguelito complex, central Mexico. Journal of South American Earth Science 95, 102311.
Torres-Sánchez, D., Verma, Sanjeet K., Barry, T.L., Verma, S.P., Torres-Hernández, J.R., 2020. $^{40}Ar/^{39}Ar$ geochronology and petrogenesis of the Sierra de San Miguelito Volcanic Complex, Mesa Central, Mexico. Lithos 370–371, 105613.
Torres-Sánchez, D., Sosa-Ceballos, G., Bolós, X., Macías, J.L., 2022. Petrogenesis of mafic-intermediate magmatism of the Michoacán-Guanajuato volcanic field in western Mexico. A geochemical review. Frontiers in Earth Science 10, 932588.
Tristán–González, M., Aguillón–Robles, A., Barboza–Gudiño, J.R., Torres–Hernández, J. R., Bellon, H., López–Doncel, R., Rodríguez–Ríos, R., Labarthe–Hernández, G., 2009. Geocronología y distribución espacial del vulcanismo en el Campo Volcánico de San Luis Potosí. Bol. Soc. Geol. Mex. 61, 287–303.
Valdez-Moreno, G., Aranda-Gómez, J.J., Ortega-Rivera, A., 2011. Geoquímica y petrología del campo volcánico de Ocampo, Coahuila, México. Boletín de la Sociedad Geológica Mexicana 63, 235–252.
Verma, S.P., 2015. Present state of knowledge and new geochemical constraints on the central part of the Mexican Volcanic Belt and comparison with the Central American Volcanic Arc in terms of near and far trench magmas. Turk. J. Earth Sci. 24, 399–1460.
Verma, S.P., Rivera-Gomez, M.A., 2013. Computer programs for the classification and nomenclature of igneous rocks. Episodes 36, 115–124.
Verma, S.P., Guevara, M., Agrawal, S., 2006. Discriminating four tectonic settings: five new geochemical diagrams for basic and ultrabasic volcanic rocks based on log-ratio transformation of major-elements data. Journal of Earth System Science 115, 485–528.
Verma, S.K., Pandarinath, K., Verma, S.P., 2012. Statistical evaluation of tectonomagmatic discrimination diagrams for granitic rocks and proposal of new discriminantfunction–based multi–dimentsional diagrams for acid rocks. International Geology Review 54, 325–347.
Verma, S.P., Pandarinath, K., Verma, S.K., Agrawal, S., 2013. Fifteen new discriminant function-based multi-dimensional robust diagrams for acid rocks and their application to Precambrian rocks. Lithos 168–169, 113–123.
Verma, S.P., Verma, S.K., Rivera-Gómez, M.A., Torres-Sánchez, D., Díaz-González, L., Amezcua-Valdez, A., Rivera-Escoto, B.A., Rosales-Rivera, M., Armstrong-Altrin, J.S., López-Loera, H., Velasco-Tapia, F., Pandarinath, K., 2018. Statistically coherent calibration of Xray fluorescence spectrometry for major elements in rocks and minerals. J. Spectrosc. 837214, 3 pages.
Verma, S.K., M. Torres, E.E., Malviya, V.P., Torres-Hernández, J.R., Torres-Sánchez, D., Rivera-Escoto, B.A., Mehta, P., 2019. Geochemistry of Mesozoic volcanic rocks from the Fresnillo area (Chilitos Formation), Zacatecas, Mexico: implications for the magma source and tectonic setting. J. South Am. Earth Sci. 96, 102311.
Verma, S.K., Torres-Sánchez, D., Hernández-Martínez, K.R., Malviya, V.P., Singh, P.K., Torres-Hernández, J.R., Rivera-Escoto, B.A., 2021. Geochemistry of Eocene felsic volcanic rocks from the Mesa Virgen-Calerilla, Zacatecas, Mexico: implications for the magma source and tectonic setting. Geol. J. 56, 3771–3790.
Verma, S.K., Torres-Sánchez, D., Sandoval-Espinel, L.C., Hernández-Martínez, K.R., Shukla, M., Torres-Sánchez, S.A., Torres Hernández, J.R., Lopéz-Loera, H., Soledad Zandomeni, P., 2023. Geochemistry, petrogenesis, and tectonic setting of the Cúcamo mafic and intermediate volcanic rocks from the Ahualulco Volcanic Complex, San Luis Potosí, Mexico. Geochemistry 83, 126015.
Zou, H., 2007. Quantitative Geochemistry. Imperial College Press, London.